White Rose Research Online

eprints@whiterose.ac.uk
https://eprints.whiterose.ac.uk
Universities of Leeds, Sheffield and York

Deposited via The University of Leeds.

White Rose Research Online URL for this paper:
https://eprints.whiterose.ac.uk/id/eprint/240598/

Version: Accepted Version

Article:
Zhang, X., Liu, J., Li, Y. et al. (2026) Erythropoietin Functionalized Hierarchical Scaffolds Enable Immunomodulated and Vascularized Bone Repair in Periodontal Defect. ACS Applied Materials & Interfaces, 18 (9). pp. 14256-14273. ISSN: 1944-8244

https://doi.org/10.1021/acsami.5c24484

This is an author produced version of an article published in ACS Applied Materials & Interfaces, made available via the University of Leeds Research Outputs Policy under the terms of the Creative Commons Attribution License (CC-BY), which permits unrestricted use, distribution and reproduction in any medium, provided the original work is properly cited.

Reuse
This article is distributed under the terms of the Creative Commons Attribution (CC BY) licence. This licence allows you to distribute, remix, tweak, and build upon the work, even commercially, as long as you credit the authors for the original work. More information and the full terms of the licence here: https://creativecommons.org/licenses/

Takedown
If you consider content in White Rose Research Online to be in breach of UK law, please notify us by emailing eprints@whiterose.ac.uk including the URL of the record and the reason for the withdrawal request.

UNIVERSITY OF LEEDS
University of Sheffield
UNIVERSITY of York

Erythropoietin Functionalized Hierarchical Scaffolds Enable Immunomodulated and Vascularized Bone Repair in Periodontal Defect

Xuan Zhang12, Jie Liu3, Yuyang Li4, Wen Li4, Deao Gu4, Yi Ting Chong5, Xuebin Yang6, FuKe Wang5, Weibin Sun12**

Author Address

[1] Department of Periodontics, Nanjing Stomatological Hospital, Affiliated Hospital of Medical School, Research Institute of Stomatology, Nanjing University, Nanjing, China

[2]The State Key Laboratory of Pharmaceutical Biotechnology affiliated to Nanjing University

[3] College of Materials Science and Engineering, Nanjing Tech University, Nanjing 211800, China

[4] Nanjing Stomatological Hospital, Affiliated Hospital of Medical School, Research Institute of Stomatology, Nanjing University, Nanjing, China

[5] Institute of Materials Research and Engineering, A*STAR (Agency for Science, Technology and Research), Fusionopolis Way, Innovis, #08-03, Singapore 138634, Republic of Singapore.

[6] Biomaterials & Tissue Engineering Group, School of Dentistry, University of Leeds, WTBB, St. James's University Hospital, Leeds LS97TF, UK

Keywords: Periodontal defects, Hierarchical porous scaffold, Polydopamine coating, Erythropoietin delivery, Vascularized osteogenesis

Abstract

The regeneration of periodontal bone is hindered by unresolved inflammation, insufficient angiogenesis, and compromised osteogenesis, conditions that are rarely addressed simultaneously by existing scaffold designs. Conventional hydrogel-based constructs often lack the mechanical robustness required for maxillofacial defects, while many synthetic scaffolds fail to replicate the multiscale pore organization essential for functional regeneration. Here, we present a dual-fabrication strategy for constructing hierarchically porous scaffolds via digital light processing (DLP)-based 3D printing of a porogen-containing resin. This hybrid approach achieves well-defined macropores for load-bearing stability and vascular infiltration, together with interconnected hierarchical micro–nanoporous that promote nutrient transport and cell–matrix interactions. To endow the scaffold with biological functionality, it was modified with polydopamine (PDA) for efficient immobilization and sustained release

of erythropoietin (EPO). The resulting scaffolds (DMPS-PDA-EPO) simultaneously regulated inflammation by promoting M2 macrophage polarization, enhanced angiogenesis through endothelial migration and tube formation, and stimulated osteogenic differentiation of human periodontal ligament stem cells under pro-inflammatory conditions. In vivo implantation in rat periodontal defect models resulted in markedly enhanced bone regeneration, with bone volume fraction and bone mineral density increasing by 161.9% and 167%, respectively, at 8 weeks compared with controls. By integrating structural precision, mechanical robustness, and immuno-angiogenic bioactivity, this EPO-functionalized hierarchical scaffold represents a clinically translatable strategy for the treatment of complex periodontal defects.

Introduction

Periodontal bone defects, frequently arising from periodontitis, trauma, or tumor resection, remain a major clinical challenge[1–3]. Unlike long bone fractures, periodontal defects develop in an inflammatory microenvironment that disrupts angiogenesis and impairs osteogenesis, often leading to incomplete or fibrotic healing[4]. Effective regeneration therefore requires scaffolds that do more than provide structural support; they must also actively modulate immune responses and promote vascularized bone formation[5].

Current clinical solutions—including autografts, allografts, and synthetic substitutes—face limitations such as donor morbidity, immune rejection, or inadequate bioactivity[6]. Tissue-engineered scaffolds have emerged as promising alternatives, yet most hydrogel-based systems lack the mechanical strength required for maxillofacial

load-bearing applications[7,8]. Moreover, many synthetic constructs fail to reproduce the multiscale porosity of native bone, which integrates macropores for vascularization, micropores for nutrient exchange, and nanoscale features for cell–matrix signaling[9–11]. Reconstructing such hierarchical organization in a mechanically robust scaffold remains a challenge. Moreover, the ability to modulate the inflammatory microenvironment of periodontal defects is also critical. Macrophages in these lesions often remain polarized toward the pro-inflammatory M1 state, which suppresses angiogenesis and osteogenesis12,13. Incorporating immunomodulatory and pro-angiogenic cues into scaffolds offers a strategy to overcome this barrier. Erythropoietin (EPO), a glycoprotein best known for regulating erythropoiesis, has recently been recognized for its pleiotropic functions in tissue repair14,15. Beyond stimulating angiogenesis, EPO promotes osteogenic differentiation and shifts macrophages toward the pro-healing M2 phenotype, making it particularly relevant for regeneration in inflamed periodontal tissues16.

Current bioactive scaffolds for bone regeneration often lose efficacy under inflammation-compromised conditions and rarely achieve coordinated regulation of immune responses, angiogenesis, and osteogenesis, particularly in periodontal and maxillofacial defects. To overcome this limitation, we developed a DLP-fabricated hierarchical micro–nanoporous scaffold with biofunctionalization for immuno-angiogenic bone repair. By employing a porogen-assisted strategy, an interconnected micro- to nanoporous network was introduced within precisely patterned macropores, thereby coupling hierarchical porosity with sufficient mechanical robustness.

Subsequent surface modification with polydopamine (PDA) enabled efficient immobilization and sustained release of EPO, yielding a scaffold that not only provides structural support and facilitates metabolic exchange but also actively modulates the inflammatory microenvironment while promoting angiogenesis and osteogenic differentiation. Unlike conventional PDA-modified or growth factor–loaded scaffolds that typically enhance isolated regenerative pathways, the present system integrates hierarchical micro–nano porosity with EPO functionalization to simultaneously regulate inflammation, vascularization, and osteogenesis under inflammatory conditions. Through systematic in vitro and in vivo investigations, we demonstrated that this multifunctional platform significantly enhances periodontal bone regeneration in inflammatory environments, highlighting its potential for clinically translatable repair of complex maxillofacial defects (Scheme 1).

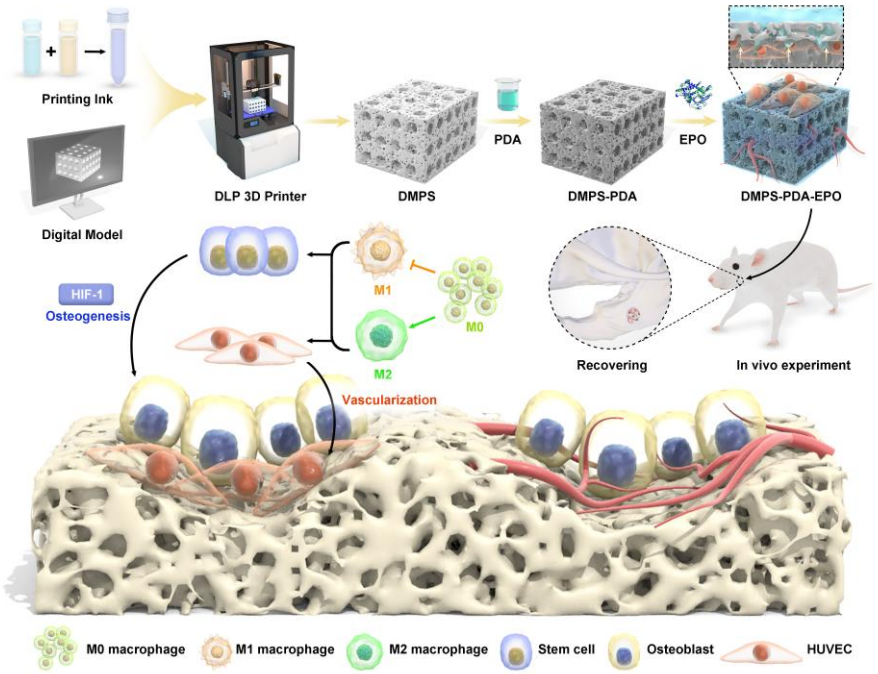

Scheme 1. Diagram depicting the fabrication process of the multifunctional scaffold and its biological mechanism in enhancing vascularization and osteogenic differentiation.

2. Experimental section

2.1 Materials

1-Octanol and ethanol were supplied by Sinopharm Chemical Reagent Co. (Shanghai, China). Bisacylphosphine oxides (BAPOs, 97% purity, molecular weight: 418.46) and di(ethylene glycol) diacrylate (DEGDA, 75% purity, molecular weight: 214.22) were purchased from Aladdin Scientific Corp (Shanghai, China), lipopolysaccharide (LPS, derived from Escherichia coli O111:B4), dexamethasone, β-glycerophosphate, and ascorbic acid were obtained from Sigma-Aldrich Co., Ltd. (Shanghai, China). Dopamine (DA, 99% purity, molecular weight: 189.64) was purchased from Xi'an Qiyue Biotechnology Co., Ltd. (China). Tris(hydroxymethyl)aminomethane hydrochloride (Tris-HCl, 10 mM, pH 8.5) was provided by Guangzhou Yitao Biotechnology Co., Ltd. (China). Recombinant human erythropoietin (EPO, 10000IU/ml/vial) was supplied by Kexing Biopharm (China). Dulbecco's modified Eagle medium (DMEM), fetal bovine serum (FBS), phosphate-buffered saline (PBS), and penicillin–streptomycin (P/S) were purchased from Gibco (USA). Endothelial cell culture medium supplemented with growth factors was obtained from ScienCell (USA).

2.2. Preparation of Materials:

115 2.2.1 Preparation and construction of DEGDA scaffolds and hierarchical micro–
116 nanoporous DEGDA scaffolds
117 Porous scaffold models were created in Shapr3D software (v3.46.1, Shapr 3D
118 Zartkoruen Mukodo Reszvenytarsasag). For in vitro testing, rectangular specimens
119 with dimensions of 5 × 4 × 2 mm were prepared, whereas cylindrical constructs (3 mm
120 diameter × 1 mm height) were fabricated for in vivo implantation studies. Dimensional
121 data were obtained directly from Shapr3D. The final designs were saved in
122 stereolithography (STL) format and subsequently processed in Chitubox slicing
123 software (China). Printing parameters were set to a layer thickness of 50 μm with an
124 exposure time of 4 s per layer.
125 The porogen system was formulated to enable the generation of hierarchical micro–
126 nanoporous DEGDA scaffolds. Briefly, the porogen mixture was composed of 50 vol%
127 1-octanol, 30 vol% ethanol, and 20 vol% deionized water, which was emulsified using
128 a high-speed disperser (FJ200-SH, Huxi, China) at 6000 rpm for 5 min. The obtained
129 porogen solution was then blended with DEGDA in different proportions (4:6, 5:5, and
130 6:4, v/v), and 1% (w/v) BAPOs photoinitiator was simultaneously introduced. The
131 mixtures were transferred into 50 mL centrifuge tubes and homogenized again at 6000
132 rpm for 5 min to prepare printable inks. Scaffold fabrication was subsequently carried
133 out using a DLP 3D printer (HF-L1, Shenzhen Hifun Technology Co., China) with a
134 405 nm UV source. After printing, the samples were washed twice by 5 min of
135 ultrasonic cleaning in absolute ethanol, followed by secondary curing. To ensure

complete removal of unreacted monomers, an additional ultrasonic treatment in ethanol for 30 min was performed.

For DEGDA scaffold preparation without microporosity, the resin solution was directly printed under the same parameters used for the microporous constructs, but without adding a porogen. Post-processing procedures were carried out identically to those applied for DMPS. Scaffolds fabricated from DEGDA with 50% porogen were designated as DMPS, while those produced from neat DEGDA without porogen were termed DPS for comparison.

2.2.2 Preparation of PDA- and EPO-modified DPS/DMPS porous scaffolds

DPS and DMPS scaffolds were first incubated in a dopamine solution (2 mg/mL in 10 mM Tris-HCl, pH 8.5) with gentle shaking at room temperature for 24 h. During this process, PDA formed via oxidative self-polymerization of dopamine in alkaline, oxygenated conditions. The samples were subsequently rinsed three times with deionized water and air-dried to yield DPS-PDA and DMPS-PDA scaffolds. For further functionalization, 5000 IU/mL of EPO was introduced onto the PDA-coated scaffolds, followed by vacuum drying to eliminate excess unbound proteins, resulting in DPS/DMPS-PDA-EPO constructs.

2.3. Characterization Evaluation of Materials:

2.3.1 Compression test

Compression testing was carried out to assess scaffold mechanics and the impact of nanoporous structures. Scaffolds were fabricated using a DLP 3D printer (designs shown in Figure S1), including both dense and porous specimens with 200 × 200 μm

158 macropores. Sample dimensions followed ASTM D1621 (12.5 × 12.5 × 25.4 mm), and
159 at least five replicates were prepared for each porogen ratio. Tests were conducted on a
160 universal testing machine under ASTM D1621 conditions, with loading applied along
161 the Z-axis at 1 mm/min. The elastic modulus was obtained from the linear region of the
162 stress–strain curve, while yield strength was defined at 1.0% offset strain. Energy
163 absorption efficiency (η) was calculated using Equation (1), representing the absorbed
164 energy relative to an ideal absorber at strain ε.

165 $$\eta = \frac{\int_0^{\varepsilon} \sigma \, d\varepsilon}{\sigma_{max} \cdot \varepsilon} \quad (1)$$

166 2.3.2 Diffusion Test

167 Diffusion behavior was examined using DLP-printed polymer sheets with varying
168 porogen contents. Uniform strips (1.5 × 6 cm, 200 μm thick) were prepared, and a
169 water-based ink marker was applied near the edge as a tracer. The strips were vertically
170 placed in deionized water, allowing the ink to migrate upward via capillary action. After
171 20 minutes, the solvent front was measured, with each test performed in triplicate for
172 consistency.

173 2.3.3 Scanning Electron Microscopy (SEM) Analysis

174 The surface morphology of the scaffolds was examined using a Hitachi Regulus 8100
175 SEM operated at 3 kV with an SE2 detector. Samples were sputter-coated with gold
176 (10 mA, 45 s) using a Quorum SC7620 prior to imaging.

177 2.4. In vitro Experiments:

178 2.4.1 Preparation of hierarchical micro–nanoporous scaffold Extracts

Hierarchical micro–nanoporous scaffold extracts were prepared according to ISO 10993-12 guidelines to ensure biosafety and standardization. In brief, scaffold samples were immersed in culture medium to obtain a stock concentration of 200 mg/mL and incubated at 37 °C for 24 h. The suspensions were then centrifuged at 2000 rpm for 5 min to remove residual particles, and the supernatant was collected. Finally, the extracts were sterilized using a 0.22 μm membrane filter and stored for later use.

2.4.2 Biocompatibility and Cell Viability Assessment

All scaffolds were sterilized by immersion in ethanol followed by ultraviolet irradiation. Cell proliferation of human umbilical vein endothelial cells (HUVECs), human periodontal ligament stem cells (hPDLSCs), and RAW 264.7 macrophages was determined using the Cell Counting Kit-8 (CCK-8, Dojindo, Japan) in accordance with the supplier's instructions. Briefly, 3×10^5 cells/well were seeded onto scaffold samples placed in 96-well plates. After treatment with 10% (v/v) CCK-8 solution for 1 h at 37 °C, absorbance at 450 nm was recorded using a microplate reader (Molecular Devices, Sunnyvale, USA). Data were processed with GraphPad Prism 9 software.

Cytotoxicity of the printed scaffolds was further investigated by live/dead staining. RAW 264.7 cells were analyzed at day 1, HUVECs at days 1 and 3, and hPDLSCs at days 1, 4, and 7. Cells were rinsed with PBS and incubated for 30 min at 37 °C in PBS containing 2 μM calcein-AM and 2 μM propidium iodide (PI, Dojindo, Japan). After washing, samples were examined using a confocal laser scanning microscope (CLSM, Nikon, Japan) with fluorescence excitation at 488 nm for live cells and 562 nm for dead cells.

2.4.3 In vitro Drug Release Evaluation

EPO release behavior was assessed using four scaffold types: DPS-EPO, DPS-PDA-EPO, DMPS-EPO, and DMPS-PDA-EPO. Samples were immersed in PBS (pH 7.4) and maintained at 37 °C to mimic physiological conditions. At predetermined intervals (days 1–7), aliquots of the supernatant were collected for analysis. The concentration of EPO released at each time point was quantified using an enzyme-linked immunosorbent assay (ELISA) kit.

2.4.4 Measurement of Intracellular Reactive Oxygen Species (ROS)

RAW264.7 macrophages were seeded in 24-well plates at a density of 5×10^4 cells/well, stimulated with LPS (250 ng/mL), and then cultured with scaffold extracts for 24 h. Intracellular ROS levels were assessed using a commercial ROS detection kit (DCFH-DA, Beyotime, China). The non-fluorescent probe DCFH-DA is oxidized by ROS into fluorescent dichlorofluorescein, with fluorescence intensity reflecting ROS accumulation. After staining with DCFH-DA followed by nuclear counterstaining with DAPI, cells were imaged under a CLSM.

2.4.5 Tube Formation Assay

For angiogenesis evaluation, 100 μL of Matrigel was added to each well of pre-chilled 96-well plates and allowed to polymerize at 37 °C for 30 min. HUVECs (1.5×10^4 cells/well) were then seeded on the Matrigel layer in medium supplemented with LPS (5 μg/mL) and scaffold extracts. Plates were incubated at 37 °C in a 5% CO_2 atmosphere for 8 h. Tubular networks were imaged, and quantitative parameters

including total tube length, branch numbers, and junctions were analyzed with ImageJ software (v1.53, NIH, USA).

2.4.6 Cell Migration Assay

HUVECs were resuspended in serum-free medium, and 2 × 10^4 cells were seeded into the upper chamber of Transwell inserts (8 μm pore size, Corning, USA). The lower chamber was filled with 800 μL of medium containing LPS (5 μg/mL) and scaffold extracts. After incubation for 24 h, non-migrated cells on the upper membrane surface were removed using a cotton swab. Cells that traversed to the lower side were fixed in 4% paraformaldehyde for 30 min, stained with 0.05% crystal violet for 15 min, and visualized under a microscope (Nikon, Japan).

2.4.7 Osteogenic Differentiation Assay

For osteogenic induction, hPDLSCs were plated in 24-well plates at a density of 2.5 × 10^4 cells per well. Once attached, the cells were cultured in an osteogenic differentiation medium supplemented with 0.1 μM dexamethasone, 10 mM β-glycerophosphate, and 50 μM L-ascorbate-2-phosphate. To mimic an inflammatory microenvironment, LPS (5 μg/mL) and scaffold extracts were introduced. The culture medium was renewed every three days. After 14 days, alkaline phosphatase (ALP) staining was carried out using an NBT/BCIP kit (Beyotime, China), and ALP activity was determined with the corresponding assay kit (Beyotime, China). For mineralization analysis, Alizarin Red S (ARS) staining was conducted after 21 days of induction to visualize calcium nodule formation. The bound ARS was subsequently eluted with 10%

(w/v) cetylpyridinium chloride, and absorbance was recorded at 562 nm using a microplate reader.

2.4.8 Quantitative Real-Time PCR Analysis

hPDLSCs were plated in 6-well plates at a density of 5×10^5 cells per well. After 24 h of incubation, the culture medium was replaced with LPS-containing medium and scaffold extracts from the respective groups. Total RNA was isolated using a RNA extraction kit, and both its concentration and purity were assessed. The purified RNA was subsequently reverse-transcribed into cDNA, followed by amplification using SYBR Green qPCR Master Mix according to the supplier's protocol. Relative mRNA levels of genes associated with macrophage polarization, angiogenesis, osteogenesis, and chemotaxis were quantified using the 2^–ΔΔCt approach. Primer sequences are listed in the Supporting Information (Table S1). For each group, at least five biological replicates were analyzed to ensure reliable quantification. Gene expression values were normalized against β-actin, which served as the internal reference.

2.4.9 Western Blot Analysis

Cellular proteins were harvested using RIPA lysis buffer (ThermoFisher Scientific, USA) and quantified with a BCA protein assay kit (Beyotime, China). Equal amounts of protein (10 μL) were resolved on 10% (w/v) SDS-PAGE gels (Smart-lifesciences, China) and subsequently transferred onto PVDF membranes (Millipore, USA). After blocking with 5% (w/v) BSA for 1 h at room temperature, the membranes were incubated with specific primary antibodies overnight at 4 °C, followed by incubation with HRP-conjugated secondary antibodies. Protein bands were detected using an

enhanced chemiluminescence substrate (Millipore, Germany). Glyceraldehyde-3-phosphate dehydrogenase (GAPDH) and α-tubulin were employed as internal loading controls for normalization.

2.4.10 RNA Sequencing

The hPDLSCs were exposed to LPS in the presence or absence of scaffold extracts for 7 days. Cells treated with LPS alone served as the control group. Total RNA was isolated using TRIzol reagent according to the manufacturer's protocol, and subsequent sequencing data were processed and analyzed via the Majorbio Cloud Platform.

2.5 In vivo Experiments

2.5.1 Animals and Surgical Procedures

All animal procedures were conducted following the ARRIVE guidelines and were approved by the Animal Ethics Committee of Nanjing University (IACUC-D2401016). The in vivo bone-forming capacity of the hierarchical micro–nanoporous scaffolds was evaluated using a rat alveolar bone defect model (male Sprague-Dawley, 6 weeks old). Rats were randomly assigned to four groups (N = 6 per group): 1) Control (no treatment), 2) DMPS scaffold, 3) DMPS-PDA scaffold, and 4) DMPS-PDA-EPO scaffold. All the prepared scaffolds were soaked in ethanol and then sterilized by ultraviolet irradiation. After one week of acclimatization, anesthesia was induced via intraperitoneal injection of pentobarbital sodium (40 mg/kg, Merck Millipore). The right cheek region was shaved, disinfcted, and a 2 cm full-thickness incision was made along the lower margin of the mandible. The masseter muscle and periosteum were carefully dissected to expose the alveolar bone adjacent to the first and second

mandibular molars. A standardized periodontal defect (3 mm diameter, 1 mm depth) was created using a round bur under saline irrigation. The periodontal fenestration defect model was selected because it is accompanied by a local inflammatory response following surgical injury, which mimics key features of inflammation-compromised bone regeneration in clinical settings. Scaffolds were implanted into the defects according to group assignment, and the incision was closed in layers. At 4 and 8 weeks post-implantation, animals were euthanized with an overdose of anesthetic, and the right mandibles were collected for histological assessment to evaluate new bone formation.

2.5.2 Micro-CT Analysis and Histology2.5.2

Micro-computed tomography (Micro-CT; SCANCO Medical AG, Switzerland) was performed at 70 kVp, 83 μA, and 6 W. After reconstruction, quantitative parameters including bone volume fraction (BV/TV), trabecular number (Tb.N), trabecular thickness (Tb.Th), trabecular separation (Tb.Sp), and bone mineral density (BMD) were analyzed for 4- and 8-week samples using CTAn software (v1.13). Following micro-CT scanning, specimens were decalcified in 10% EDTA (w/v) for 4 weeks and then embedded in paraffin, oriented parallel to the section plane. Serial cross-sections were prepared and stained with Hematoxylin & Eosin (H&E) and Masson's trichrome according to standard protocols. Immunohistochemical analysis was conducted to evaluate the expression of CD86 (#ab15323, Abcam, UK), CD206 (#ab64693, Abcam, UK), osteocalcin (OCN, GB120012-50, Servicebio, China), and vascular endothelial growth factor (VEGF, P15692, Proteintech, USA).

309 2.6 Statistical Analysis2.6

310 All experiments were conducted in triplicate, and data are expressed as mean ±
311 standard deviation (SD). Statistical comparisons were carried out using SPSS software
312 (version 22.0, IBM Corp., Armonk, USA). One-way analysis of variance (ANOVA)
313 followed by LSD post-hoc tests was applied to determine differences among groups. A
314 p-value less than 0.05 was considered statistically significant.

315 Results and Discussions

316 3.1. Cooperative Effects of Macro- and Micro-Porosity on Scaffold Function:
317 Mechanical Energy Absorption and Pore Connectivity

318 A dual-fabrication strategy was employed to engineer a hierarchically porous
319 DEGDA scaffold, in which macropores were patterned by DLP-based 3D printing and
320 micropores were introduced through an alcohol-based porogen system (1-octanol,
321 ethanol, and water). The resulting architecture combined ordered macropores (~200
322 μm) that facilitate tissue ingrowth and vascular invasion with interconnected
323 micropores ranging from tens of nanometers to several micrometers, which enhance
324 nutrient diffusion, cell migration, and endothelial infiltration—critical processes for
325 osteogenesis and angiogenesis.17 Unlike conventional phase-separation methods that
326 often generate isolated voids, the porogen-assisted approach yielded a continuous
327 microporous network, thereby more closely mimicking the hierarchical porosity of
328 native bone and improving scaffold biofunctionality.18,19 20

329 The influence of porogen concentration was systematically examined by fabricating
330 scaffolds with 40%, 50%, and 60% porogen. All scaffolds exhibited the characteristic

stress–strain behavior of porous constructs, including an initial elastic region followed by stress fluctuations caused by strut collapse.21 Increasing porogen content significantly reduced compressive strength (71 MPa at 40%, 23 MPa at 50%, and 11 MPa at 60%), reflecting the trade-off between porosity and polymer density (Figure 1A). Importantly, despite porogen addition, the 200 μm macropore framework was consistently preserved, confirming the fidelity of the DLP process (Figure 1B, 1C).

The influence of macropores (fabricated by 3D printing) on the mechanical behavior was elucidated by comparing solid and macroporous scaffolds. The introduction of macropores significantly increased the strain at failure, demonstrating improved flexibility. As shown in Figure 1D (and Figure S2), analyses of energy absorption and energy absorption efficiency indicated that macroporous scaffolds dissipated considerably more mechanical energy than their solid counterparts—a desirable attribute for load-bearing bone applications, as it helps alleviate stress shielding and enhances implant durability. Furthermore, when comparing scaffolds with and without porogen (i.e., with or without micropores, Figure 1D), those containing porogen exhibited even higher energy absorption efficiency than pure DEGDA, highlighting the synergistic contribution of interconnected micro- and macropores to mechanical energy dissipation.

Gas permeability and dye diffusion assays demonstrated that scaffolds with ≥50% porogen formed a highly interconnected microporous network, supporting rapid transport of water, oxygen, and small molecules. The neat DEGDA film (2 mm thickness) displayed limited gas transport, with a measured transmission rate of

20.268 ml/(m²·day) at 1 atm, 23 °C, and 0 ± 3% relative humidity. In contrast, all porogen-containing scaffolds exhibited permeability beyond the detection limits, allowing gas to traverse almost immediately. This pronounced transport capability is attributed to the formation of a highly interconnected microporous network, which provides continuous, unobstructed channels for diffusion. Dye diffusion assays further confirmed that scaffolds with ≥50% porogen exhibited significantly greater pore interconnectivity, with solvent and dye readily traversing the films. Figure 1E and 1F shows the dye diffusion assay using 0.2 mm-thick polymer sheets as thin-layer chromatography (TLC) analogs. The sheet with 40% porogen displayed slower solvent migration while sheets prepared with 50% and 60% porogen exhibited substantially faster diffusion, suggesting that increased porogen content promotes the formation of a more interconnected pore network. Moreover, as shown in Figure S3 and S4, both solvent and dye can rapidly penetrate through polymer films with higher porogen content, confirming the existence of a three-dimensional, interconnected porous network. These results indicate that porogen concentrations above 50% generate a continuous pore structure capable of supporting the transport of water, oxygen, and small molecules throughout the scaffold. Considering its compressive strength within the physiological range of alveolar bone (3–30 MPa)22 and the favorable micropore interconnectivity, the 50% porogen DEGDA formulation was chosen for subsequent scaffold fabrication.

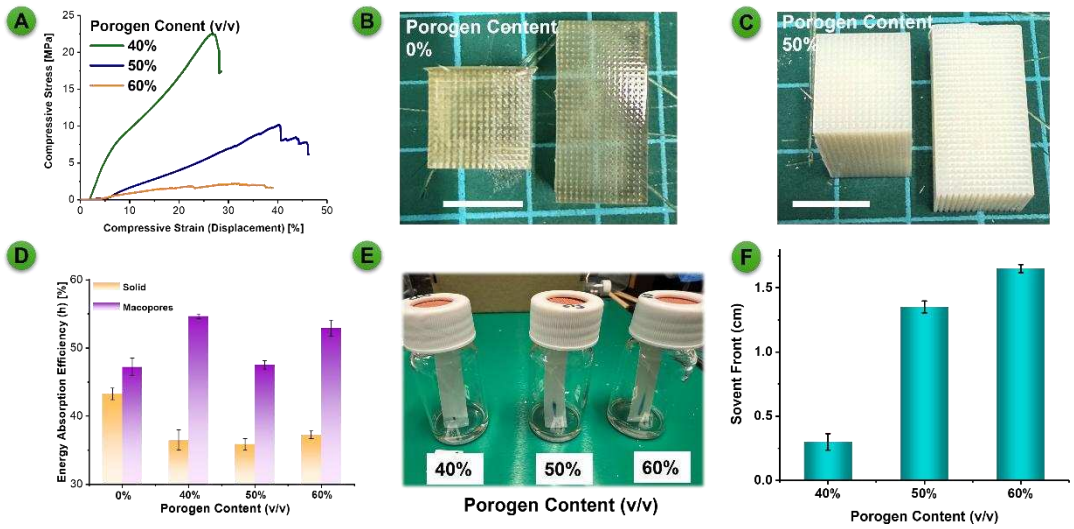

373

374 **Figure 1. Synergistic effects of macro- and micropores on scaffold performance.**

375 (A) Compressive stress–strain curves of 3D-printed scaffolds with 200 μm macropores

376 and varying porogen contents (40%, 50%, and 60% v/v). (B, C) Photographs of

377 scaffolds printed with 200 μm macropores using DEGDA without porogen (B) and with

378 50% porogen (C). (D) Energy absorption efficiency of scaffolds with and without

379 200 μm macropores across different porogen concentrations. (E) Water-based ink

380 spread on polymer sheets (0.2 mm thickness) printed from DEGDA with different

381 porogen contents. (F) Quantification of solvent front progression on polymer sheets

382 printed from DEGDA with varying porogen levels. Scale bars in (B) and (C): 1 cm.

383 3.2. Structural and Biological Evaluation of PDA-Functionalized Hierarchical

384 Micro–nanoporous Scaffolds

385 Scaffolds were fabricated via DLP printing with defined macropores (~200 μm) and

386 dimensions of 1 × 2.5 × 4 mm, using either neat DEGDA resin (DPS) or DEGDA with

387 50% (v/v) porogen (DMPS). Micro-CT imaging confirmed that both scaffold types

388 exhibited precise, interconnected macroporous architectures, validating the accuracy of

the printing process (Figure S5). Subsequent PDA coating by in situ polymerization gave DPS-PDA and DMPS-PDA, enabling surface bioactivation without altering structural fidelity.

SEM imaging revealed obvious differences between the printed scaffolds: DPS exhibited smooth surfaces, whereas DMPS displayed a hierarchical micro–nano porous network (average pore size ~300 nm) arising from porogen removal, which is advantageous for nutrient diffusion and cell migration (Figure 2A)23. PDA deposition preserved pore morphology, though more particulate deposition was observed on DPS surfaces, likely due to limited infiltration compared to the interconnected micropores of DMPS24,25. Pore size distribution (Figure 2B) and BET analysis further confirmed that PDA functionalization did not significantly alter microporosity, with DMPS and DMPS-PDA showing porosities of ~69%.

Both micropores and PDA coatings enhanced hydrophilicity, as demonstrated by progressive decreases in water contact angle from DPS (35.4°) to DPS-PDA (31.8°), DMPS (27.5°), and DMPS-PDA (22.3°) (Figure S6). As shown in Figure 2C, FTIR spectra confirmed PDA deposition via characteristic O–H, N–H, and aromatic C=C signals. Long-term degradation studies (Figure 2D,) up to 24 weeks showed greater mass loss in DMPS and DMPS-PDA compared to DPS and DPS-PDA, attributable to increased surface area and water penetration, suggesting improved resorption potential for hierarchical micro–nanoporous scaffolds. The observed gradual degradation behavior suggests that the scaffold can provide temporary mechanical support during early periodontal healing while progressively permitting in vivo resorption and

411 remodeling to accommodate vascularized bone ingrowth. It should be noted that while
412 pH variation during scaffold degradation was monitored and remained stable under
413 physiological conditions (Figure S7), direct zeta potential measurement was not
414 performed, as the DMPS-based scaffolds are bulk three-dimensional constructs rather
415 than dispersed particulate systems; therefore, surface charge–related effects were
416 instead inferred from PDA functionalization, wettability changes, and consistent
417 biological responses, which collectively reflect the electrochemical characteristics of
418 the scaffold surface.

419 Biological performance was evaluated using CCK-8 assays to assess scaffold
420 cytotoxicity toward HUVECs and hPDLSCs. On day 1, all groups showed comparable
421 viability; by day 3, DPS and DPS-PDA exhibited reduced viability, while DMPS and
422 DMPS-PDA maintained levels like the control (Figure S8A, S8D), indicating superior
423 cytocompatibility of hierarchical micro–nanoporous scaffolds. Live/dead staining
424 (Figure 3A, S8B, S9 and S8E) and cytoskeleton visualization (Figure 3B and Figure
425 S10) confirmed enhanced adhesion and survival of HUVECs (3 days) and hPDLSCs (7
426 days) on DMPS and DMPS-PDA, with well-organized F-actin and a higher proportion
427 of viable cells.

428 Cell adhesion at 4 and 24 h (Figure S8C, S8F) showed markedly greater early
429 attachment on DMPS and DMPS-PDA (≈36%) than on DPS and DPS-PDA (≈17%),
430 with adhesion exceeding 70% by 24 h for DMPS-derived scaffolds. CLSM images
431 further confirmed these results, showing pronounced pseudopodial extension on
432 hierarchical micro–nanoporous surfaces, which serve as crucial intracellular cues for

stem cell differentiation26. These results indicating that microporosity promotes cell anchoring and spreading27, and that PDA functionalization further enhances adhesion, consistent with Ghorai et al28. Overall, DMPS scaffolds—especially with PDA modification—exhibited excellent surface properties, hydrophilicity, and cytocompatibility, supporting their use in further functional studies.

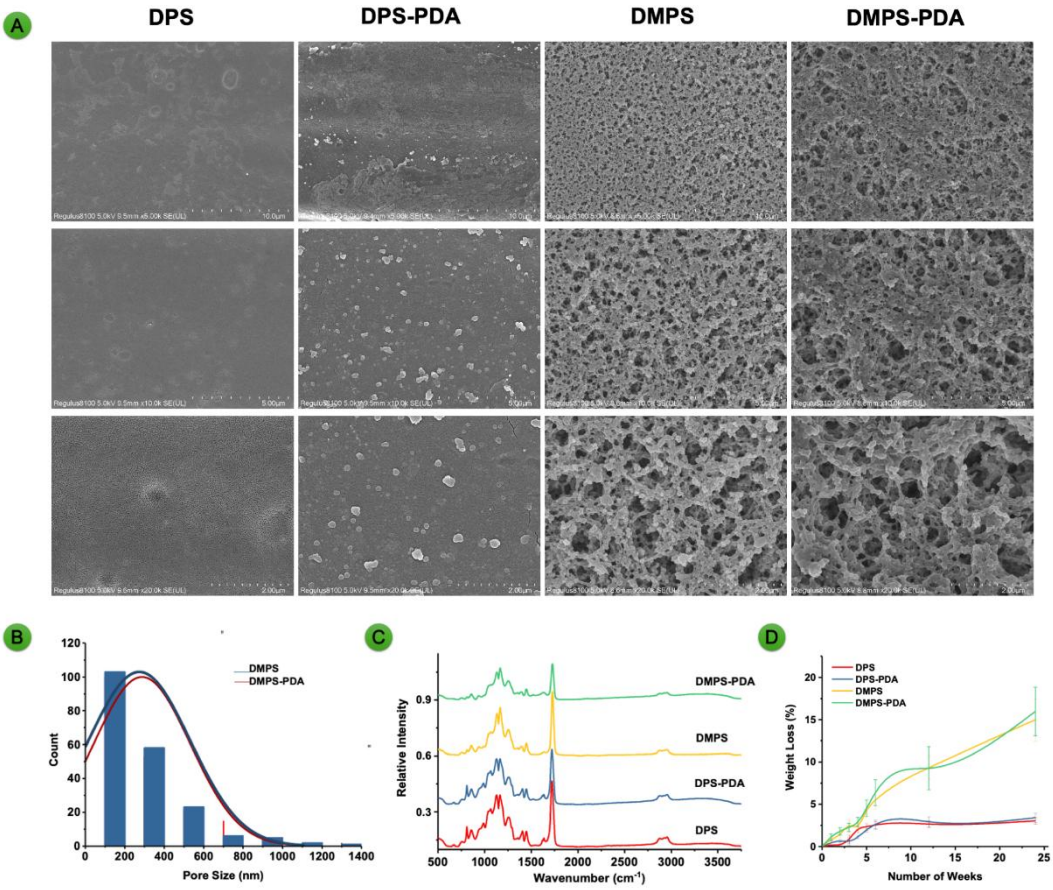

Figure 2. Structural and biological evaluation of PDA-functionalized hierarchical micro–nanoporous scaffolds. (A) Cross-sectional SEM images illustrating scaffold morphology. (B) Comparison of pore size distributions for DMPS before and after PDA coating (inset shows the distribution at a larger scale). (C) FTIR spectra of printed scaffolds pre- and post-PDA modification. (D) Analysis of scaffold degradation rates over time. Data are presented as mean ± SD (n = 3).

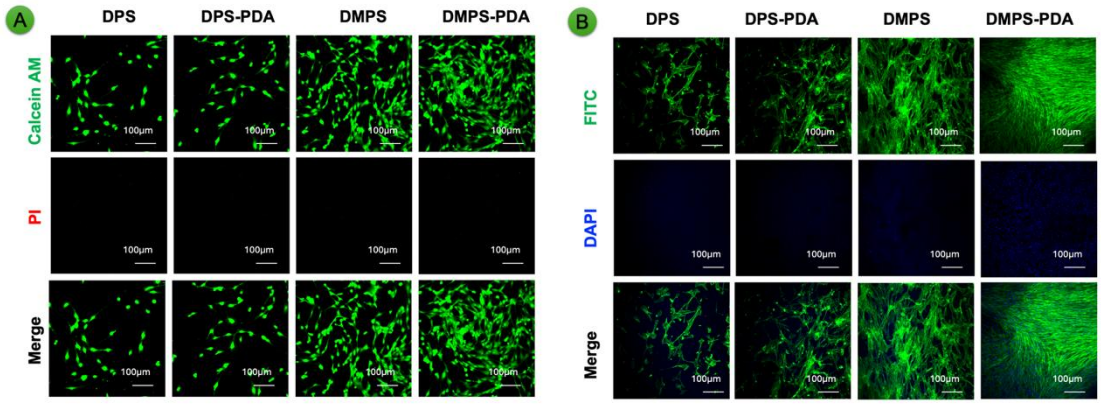

Figure 3. Live/dead staining and cytoskeleton visualization. (A) Representative live/dead staining images of hPDLSCs. (B) Fluorescence images showing nuclei (blue) and cytoskeleton (green) of hPDLSCs.

3.3. Characterization and cytocompatibility of DMPS-PDA-EPO scaffolds

SEM images (Figure 4A) showed that EPO incorporation did not alter the scaffold's porous architecture. At higher magnification, granular aggregates were observed on DMPS-PDA surfaces, likely representing EPO deposition. FTIR spectra confirmed sequential modification, with DMPS-PDA exhibiting amine and catechol peaks, and DMPS-PDA-EPO showing additional amide and hydroxyl signals, verifying successful EPO integration (Figure 4B). Our results are also in accordance with a previous study that loaded EPO onto a silk fibroin/collagen/hydroxyapatite scaffold29. EPO loading and release profiles were analyzed by ELISA over 7 days. Non-microporous scaffolds (DPS-EPO, DPS-PDA-EPO) displayed a burst release of 76.6% and 61.8% within 24 h, reaching 94.2% and 86.1% by day 7 (Figure 4C). In contrast, hierarchical micro–nanoporous scaffolds (DMPS-EPO, DMPS-PDA-EPO) exhibited sustained release, with 29.7% and 21.9% released on day 1 and cumulative release of 69.8% and 57.9%

by day 7, indicating that micro-nano porosity and PDA coating effectively reduced the burst effect. The nanopore structure of biomaterial scaffolds not only influences cellular behaviors—such as the topographical response involved in cell adhesion—but also provides a larger specific surface area that facilitates the adsorption and anchoring of bioactive molecules, thereby enabling sustained drug release30. Moreover, the synergistic interaction between the mussel-inspired properties of PDA and the micro-nanoporous architecture further amplifies this effect31. CCK-8 assays (Figure S11) confirmed high cytocompatibility across all groups. SEM (Figure 4D) and cytoskeletal imaging (Figure 5) revealed enhanced attachment and spreading of hPDLSCs on DMPS-PDA and DMPS-PDA-EPO scaffolds, where cells exhibited elongated pseudopodia and organized morphology, indicating that micro-nano porosity and PDA functionalization promote adhesion, while the incorporation of EPO did not compromise cellular compatibility. Collectively, the structural robustness, bio-functional stability, and compatibility with standard clinical sterilization protocols position the DMPS-PDA-EPO scaffold as a highly translatable platform for inflammation-compromised bone regeneration.

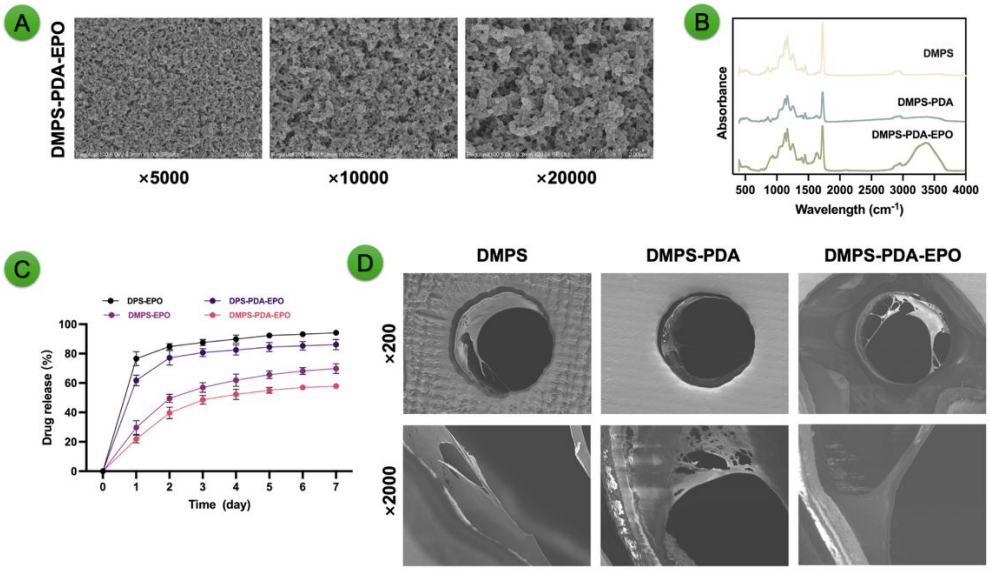

Figure 4. Structural features and cytocompatibility assessment of DMPS-PDA-EPO scaffolds. (A) SEM micrographs of the DMPS-PDA-EPO scaffold. (B) FT-IR spectra comparing DMPS, DMPS-PDA, and DMPS-PDA-EPO scaffolds. (C) Cumulative EPO release curves from different scaffold groups. (D) SEM images of hPDLSCs after 7 days of culture on DMPS, DMPS-PDA, and DMPS-PDA-EPO scaffolds. Data are presented as mean ± SD (n = 3).

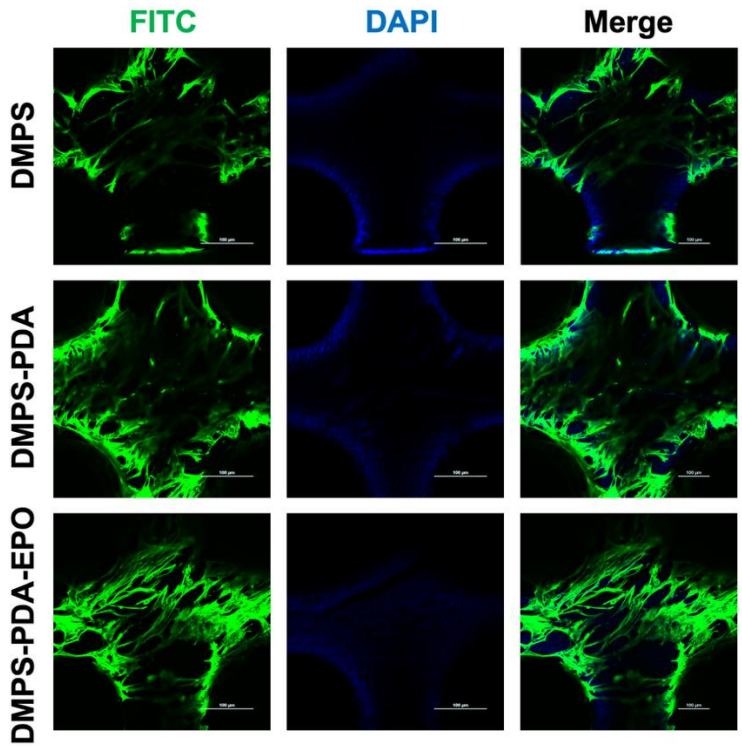

Figure 5. Cytoskeletal staining of hPDLSCs after 7 days of culture on DMPS, DMPS-PDA, and DMPS-PDA-EPO scaffolds.

3.4. Modulation of Inflammation and Macrophage Polarization by DMPS-PDA-EPO

Macrophage polarization plays a pivotal role in regulating inflammation and is closely associated with oral diseases such as periodontitis and periapical lesions, where persistent inflammation accelerates alveolar bone loss32. The murine RAW 264.7 cell line, widely used in immunological and biomaterials research, serves as a standard model for studying macrophage behavior33. Owing to their phenotypic plasticity, macrophages can adopt distinct functional states in response to microenvironmental cues, profoundly influencing inflammatory progression and bone remodeling34.

To evaluate the immunomodulatory effects of DMPS-PDA-EPO scaffolds, qRT-PCR was conducted to analyze inflammatory gene expression. As shown in Figure 6, LPS

stimulation significantly upregulated pro-inflammatory markers including interleukin-1 beta (IL-1β), cyclooxygenase-2 (COX-2) and interleukin-6 (IL-6) ($p < 0.05$), whereas DMPS-PDA-EPO treatment markedly suppressed their expression while enhancing anti-inflammatory genes including interleukin-10 (IL-10), arginase-1 (Arg-1) and transforming growth factor-beta (TGF-β) ($p < 0.05$). Given the dual roles of M1 (pro-inflammatory, tissue-destructive) and M2 (anti-inflammatory, pro-regenerative) macrophages, modulating macrophage polarization via biomaterial design represents an effective strategy to regulate immune responses and enhance tissue regeneration35. These findings indicate that LPS drives RAW 264.7 cells toward a pro-inflammatory M1 phenotype, while PDA-modified scaffolds—particularly DMPS-PDA-EPO—attenuate M1 activation and promote M2 polarization.

Inflammatory processes are strongly linked to the overproduction of ROS, which accelerate alveolar bone resorption and hinder tissue repair36. To assess intracellular ROS levels, fluorescence intensity was measured. Upon LPS stimulation, markedly elevated ROS fluorescence was detected in both the PBS and DMPS groups. Conversely, scaffolds modified with PDA or further functionalized with EPO significantly attenuated ROS generation, with the latter showing the most pronounced antioxidative effect ($p < 0.05$) (Figure 7A). Consistent results were obtained through immunofluorescence staining, demonstrating that DMPS-PDA-EPO effectively limited ROS accumulation. These outcomes indicate that PDA-coated scaffolds inherently confer antioxidant activity, which is further amplified by EPO incorporation.

The anti-inflammatory potential of EPO-functionalized scaffolds was further examined by assessing tumor necrosis factor-alpha (TNF-α) expression. As shown in Figure 7B, LPS stimulation markedly increased TNF-α fluorescence in PBS and DMPS groups, while DMPS-PDA and DMPS-PDA-EPO scaffolds substantially suppressed its expression, with the latter exhibiting the lowest fluorescence intensity ($p < 0.05$).

Collectively, these results demonstrate that DMPS-PDA-EPO scaffolds mitigate oxidative stress, suppress pro-inflammatory cytokine secretion, and regulate macrophage polarization, highlighting their therapeutic potential for controlling inflammation-induced alveolar bone resorption.

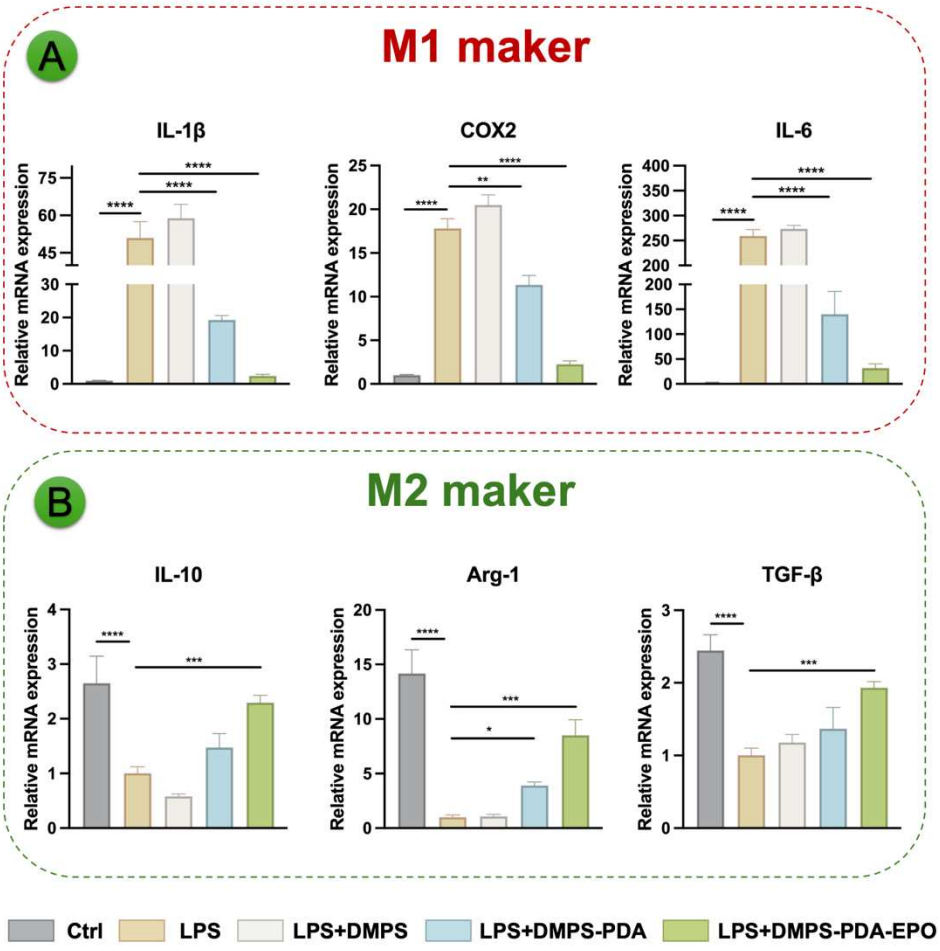

Figure 6. Modulation of inflammatory responses and macrophage polarization by DMPS-PDA-EPO scaffolds. (A) mRNA levels of M1-associated genes (IL-1β, COX-2, IL-6) in RAW264.7 cells assessed by qRT-PCR. (B) Expression of M2-associated genes (IL-10, Arg-1, TGF-β) determined by qRT-PCR. Data are presented as mean ± SD (n = 3). *$p < 0.05$, **$p < 0.01$, ***$p < 0.001$, ****$p < 0.0001$ compared with the LPS-treated group.

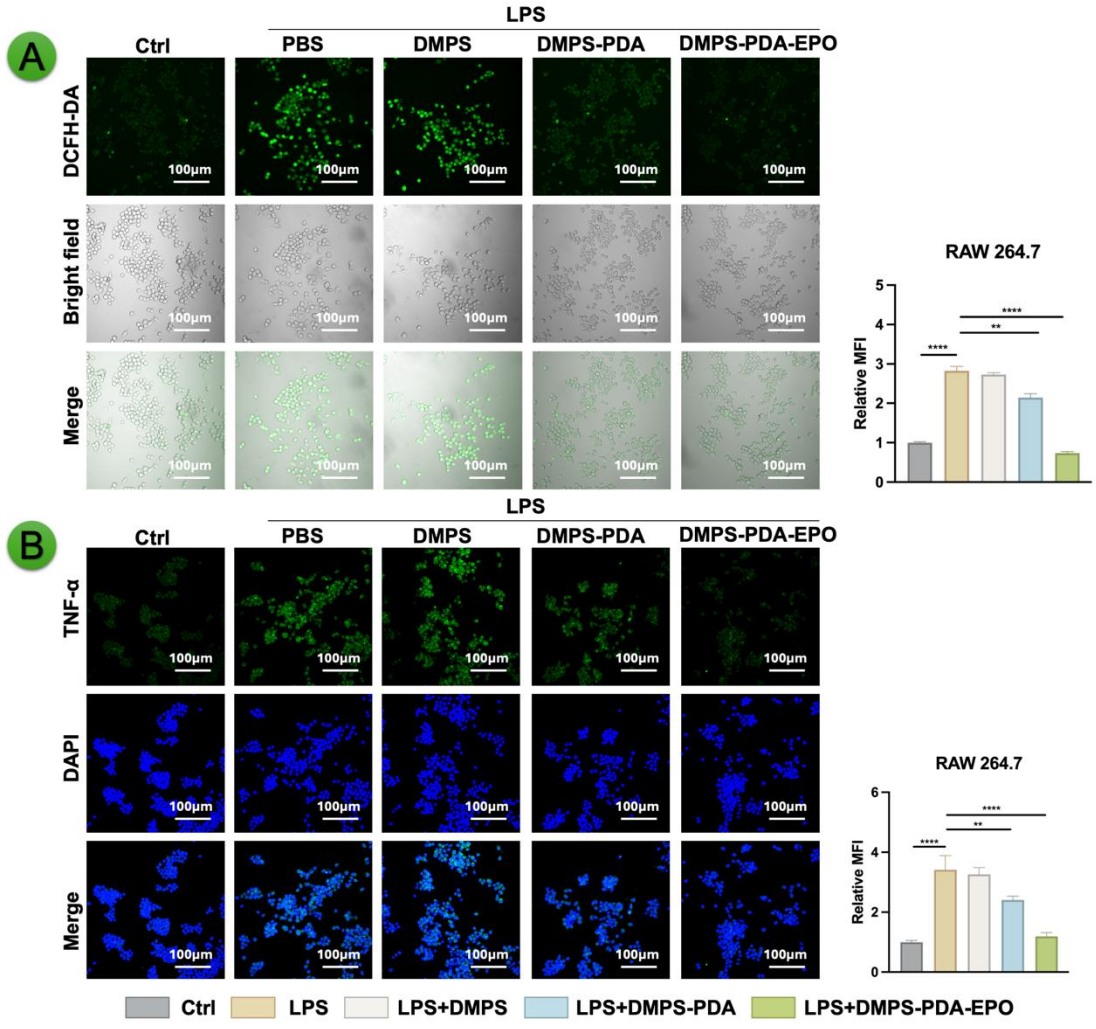

Figure 7. Immunomodulatory effects of DMPS-PDA-EPO scaffolds on macrophage inflammatory responses. (A) Intracellular ROS production detected by DCFH-DA staining, visualized by immunofluorescence, and quantitatively analyzed. (B)

539 Immunofluorescence staining of TNF-α in RAW264.7 cells, with corresponding
540 quantitative analysis. Data are presented as mean ± SD (n = 3). **$p < 0.01$, ***$p <$
541 0.001, ****$p < 0.0001$ compared with the LPS-treated group.

542 3.5. DMPS-PDA-EPO promotes angiogenesis in HUVECs

543 Bone is a metabolically active tissue with abundant vasculature, allowing continuous
544 remodeling to maintain structural integrity37. Effective bone regeneration requires
545 sufficient neovascularization to support osteoid deposition and matrix formation.
546 Hierarchical interconnected porosity plays a key role by providing both mechanical
547 stability and a microenvironment favorable for endothelial proliferation and
548 vascularization38.

549 Directed migration of endothelial cells is fundamental to angiogenesis39. To evaluate
550 the pro-angiogenic potential of DMPS-PDA-EPO scaffolds under inflammatory stress,
551 HUVEC motility was examined using scratch and Transwell assays. LPS exposure
552 markedly inhibited migration, whereas extracts from DMPS-PDA and DMPS-PDA-
553 EPO scaffolds restored both horizontal and vertical migration, with the EPO-loaded
554 group showing the strongest recovery ($p < 0.05$) (Figure 8A, S12).

555 Consistent with the migration results, tube formation assays (Figure S13) revealed
556 that LPS exposure markedly impaired angiogenic capacity, as evidenced by a reduction
557 in nodes, junctions, segments, branch length, master segments, and mesh structures.
558 Remarkably, treatment with DMPS-PDA-EPO extracts restored vascular network
559 formation, achieving levels comparable to or even surpassing those observed in the
560 untreated control group. Quantitative assessment confirmed that DMPS-PDA-EPO

561 significantly enhanced all tube formation parameters relative to both the LPS group and
562 other scaffold groups ($p < 0.05$), underscoring its strong pro-angiogenic and anti-
563 inflammatory potential (Figure S14). To further explore the underlying mechanisms,
564 gene expression analysis was conducted (Figure S15). LPS challenge significantly
565 suppressed the transcription of chemokines such as C-C motif chemokine ligand
566 (CCL)-2, CCL8, and CCL21, all of which are critical regulators of endothelial
567 recruitment and motility ($p < 0.05$). Notably, DMPS-PDA-EPO treatment effectively
568 reversed this suppression, leading to a marked upregulation of these genes ($p < 0.05$),
569 thereby providing molecular evidence for its ability to restore angiogenic signaling
570 pathways.

571 Similarly, LPS stimulation led to a pronounced downregulation of VEGF, basic
572 fibroblast growth factor (bFGF), and ephrin-B4 receptor (EphB4), all of which are
573 pivotal regulators of angiogenesis (Figure 8B). Treatment with DMPS-PDA-EPO
574 significantly restored the expression of these angiogenic markers ($p < 0.05$). At the
575 protein level, Western blot analysis confirmed the same trend, further validating these
576 findings (Figure 8C, S16). Taken together, these results demonstrate that DMPS-PDA-
577 EPO effectively counteracts LPS-induced suppression of angiogenic signaling,
578 reinstates endothelial cell activity, and enhances neovascularization, underscoring its
579 therapeutic promise for bone defect repair in inflammatory environments.

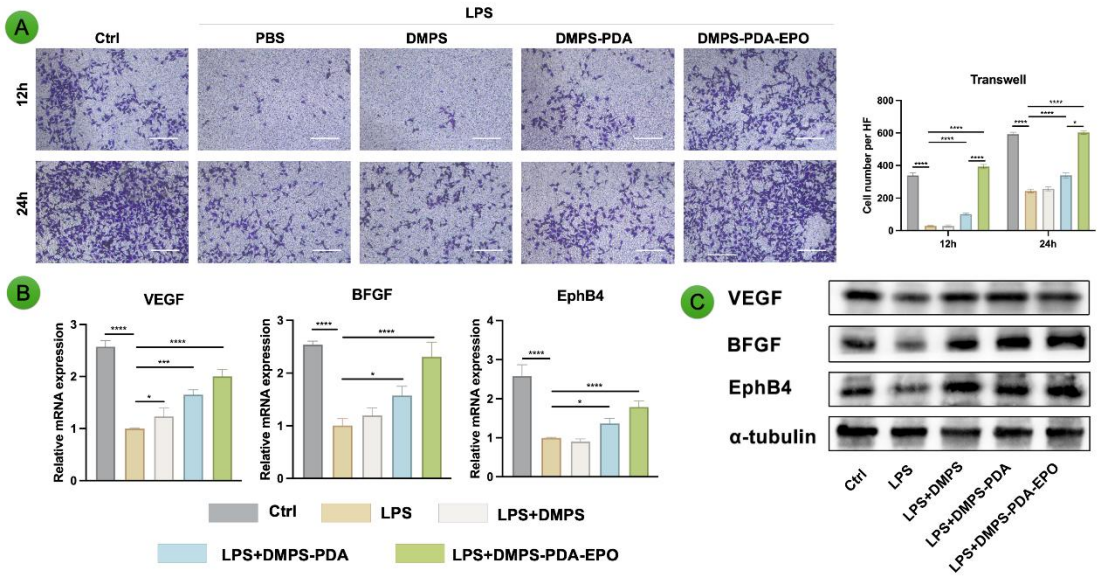

Figure 8. Angiogenic effects of DMPS-PDA-EPO on HUVECs. (A) Transwell migration assay showing HUVECs that penetrated the membrane after 12 and 24 h of culture with scaffold extracts (left) and corresponding quantification (right). (B) qRT-PCR evaluation of angiogenic markers (VEGF, bFGF, and EphB4). (C) Western blot of VEGF, bFGF, and EphB4 expression after 48 h. Scale bar = 400 μm. Data are presented as mean ± SD (n = 3). *$p < 0.05$, **$p < 0.01$, ***$p < 0.001$, ****$p < 0.0001$.

3.6. DMPS-PDA-EPO Promotes Osteogenic Differentiation of hPDLSCs Under Inflammatory Conditions via HIF-1 Signaling

EPO, originally identified as a hematopoietic growth factor, also possesses potent anti-inflammatory, antioxidant, and anti-apoptotic properties, while promoting local microvascular perfusion—attributes that support its therapeutic potential in tissue regeneration40. Recent studies have further demonstrated its role in stimulating osteogenic differentiation and bone formation41,42. To evaluate its osteogenic effects

under inflammatory stress, hPDLSCs—key stem cells for alveolar bone regeneration—were exposed to LPS to simulate inflammation-induced suppression of osteogenesis43.

Scaffold extracts from DMPS-PDA and DMPS-PDA-EPO both alleviated the inhibitory effects of LPS, with the EPO-loaded group showing the strongest recovery. In contrast, unmodified DMPS exhibited limited benefit. ALP staining revealed markedly reduced activity after LPS treatment (Figure 9A), while DMPS-PDA-EPO significantly restored ALP intensity and enzymatic activity compared with the LPS group ($p < 0.05$) (Figure S17A), indicating effective recovery of early osteogenic potential. The formation of mineralized nodules marks late-stage osteogenic differentiation. After 21 days of induction, LPS-induced inflammation markedly impaired calcium nodule formation in hPDLSCs, whereas DMPS-PDA-EPO treatment effectively alleviated this inhibition and restored mineral deposition (Figure 9B, S17B). RT-qPCR analysis further showed that LPS suppressed osteogenic genes, including ALP, bone morphogenetic protein 2 (BMP2), runt-related transcription factor 2 (RunX2) and OCN, while DMPS-PDA-EPO significantly upregulated their expression beyond that of the DMPS group ($p < 0.05$) (Figure 9C). Consistently, western blotting confirmed enhanced BMP2, RUNX2, and OCN protein levels after DMPS-PDA-EPO treatment, demonstrating its ability to counteract inflammation and promote osteogenic maturation (Figure 9D, S18).

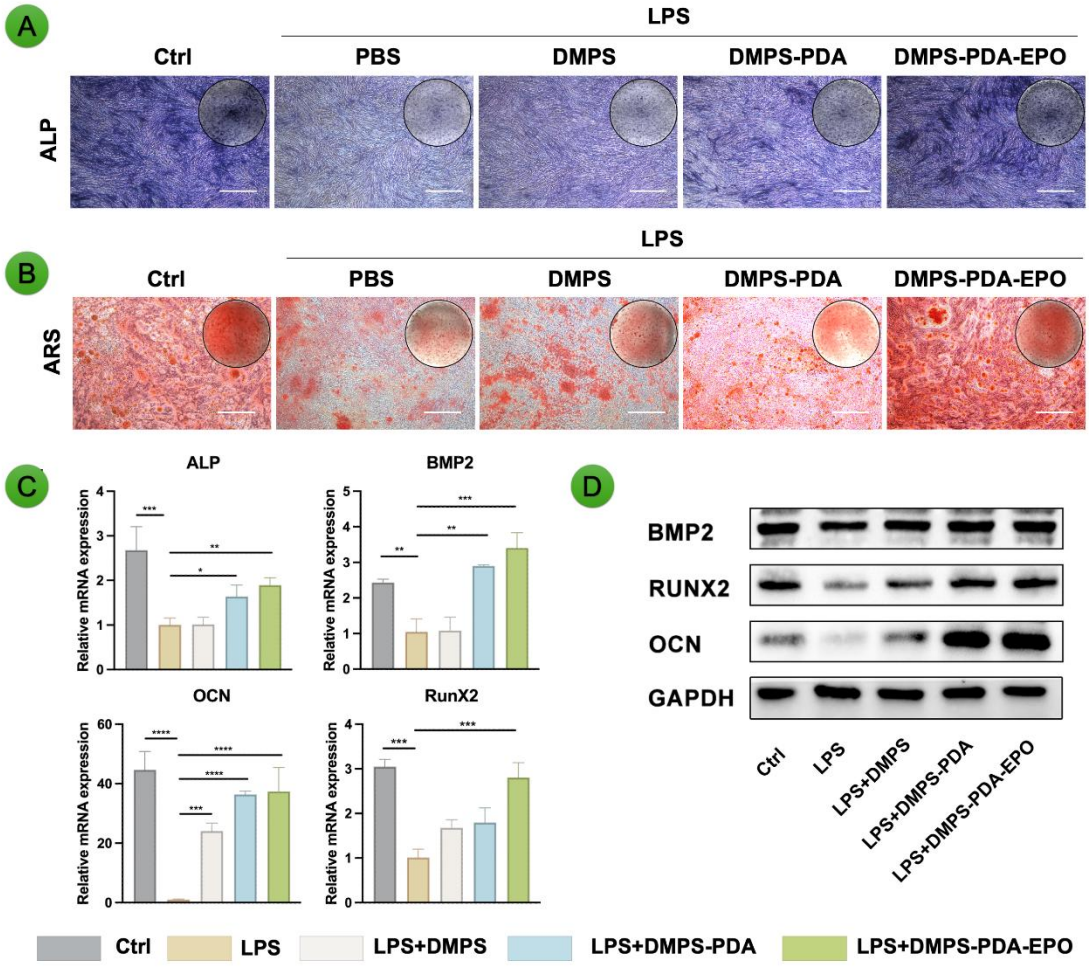

613

614 Figure 9. DMPS-PDA-EPO Promotes Osteogenic Differentiation of hPDLSCs. (A)
615 ALP staining of hPDLSCs. (B)ARS staining of mineralized nodules. (C) Gene
616 expression analysis of osteogenic markers (ALP, BMP2, RunX2, and OCN) in
617 hPDLSCs by qRT-PCR. (D) Western blot and semi-quantitative analysis of osteogenic
618 proteins (BMP2, RunX2, and OCN) after 7 days. Scale bar = 400 μm. All data are
619 presented as mean ± SD (n = 3). * $p < 0.05$, ** $p < 0.01$, and *** $p < 0.001$ relative to
620 the LPS-treated group.

621 To investigate the molecular mechanisms driving the pro-osteogenic effects of
622 DMPS-PDA-EPO under inflammatory conditions, RNA-Seq analysis was performed

on LPS-stimulated hPDLSCs with or without DMPS-PDA-EPO treatment. This analysis identified 523 differentially expressed genes (DEGs) ($p < 0.05$, $|\log_2 FC| > 1$), comprising 182 upregulated and 341 downregulated genes (Figure 10A).

Subsequently, gene ontology (GO) enrichment analysis was carried out to classify these DEGs into biological processes (BP), cellular components (CC), and molecular functions (MF) (Figure 10B). Within the MF category, DEGs were significantly enriched in protein binding, extracellular matrix (ECM) structural constituents, and calcium ion binding. The CC category highlighted ECM (GO:0031012), external encapsulating structure (GO:0030312), and collagen-containing ECM (GO:0062023), indicating scaffold-mediated ECM remodeling. For the BP category, enriched terms included developmental processes (GO:0032502), ECM organization (GO:0030198), and regulation of calcium ion transport (GO:0051924), all of which are closely associated with osteogenic differentiation.

Kyoto encyclopedia of genes and genomes (KEGG) pathway analysis identified several significantly enriched signaling pathways (Figure 10C), with the hypoxia-inducible factor 1 (HIF-1) pathway emerging as the most prominently enriched. The HIF-1 pathway plays a pivotal role in hypoxia-driven osteoblast differentiation and survival and has been previously linked to EPO-mediated enhancement of osteogenesis50. Additional enriched pathways included phosphoinositide 3-kinase – protein kinase b (PI3K-Akt), TNF, and mitogen-activated protein kinase (MAPK) signaling, which are well-established regulators of cell proliferation, survival, inflammatory responses, and osteogenic differentiation. Moreover, pathways related to

extracellular matrix remodeling, such as focal adhesion and regulation of the actin cytoskeleton, were also enriched, suggesting improved cellular support for differentiation and tissue regeneration.

Overall, these results suggest that DMPS-PDA-EPO promotes osteogenic differentiation of LPS-impaired hPDLSCs mainly through HIF-1 activation, accompanied by modulation of ECM remodeling and inflammatory pathways. It should be noted that the enrichment of the HIF-1 signaling pathway identified by RNA-seq and KEGG analyses reflects a pathway association rather than definitive mechanistic evidence, and further pathway-specific validation would be required to establish direct causality.

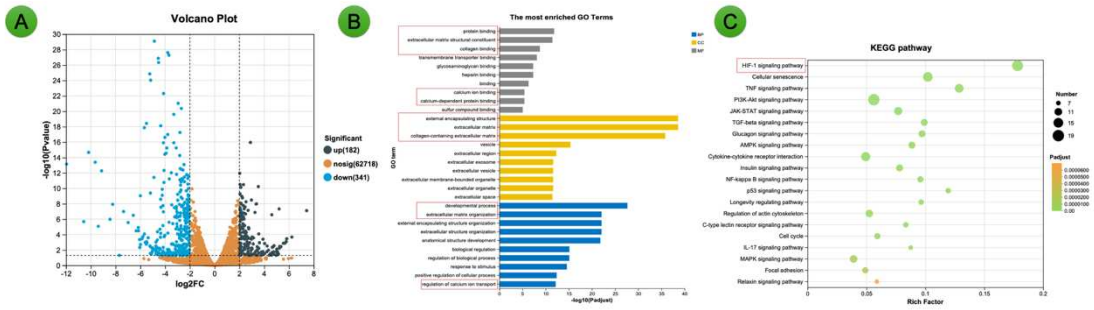

Figure 10. DMPS-PDA-EPO Promotes Osteogenic Differentiation of hPDLSCs Under Inflammatory Conditions via the HIF-1 Signaling Pathway. (A) Volcano plot of differentially expressed genes. (B) GO enrichment analysis of hPDLSCs treated with LPS + DMPS-PDA-EPO extracts; the top 25 significant terms are displayed, with biological processes, cellular components, and molecular functions shown in blue, yellow, and gray, respectively. (C) KEGG pathway enrichment analysis comparing LPS + DMPS-PDA-EPO–treated cells to the LPS group.

3.7. In Vivo Evaluation of DMPS-PDA-EPO in Promoting Bone Regeneration in a Rat Periodontal Fenestration Model

For the in vivo experiments, a rat periodontal fenestration defect model was established by surgically removing a portion of the alveolar bone, a commonly employed method for investigating scaffold-mediated bone regeneration. This validated model enables reliable evaluation of the scaffold's capacity to support tissue repair and regeneration44. In this study, standardized 3 mm defects were created in the alveolar bone of rats. The regenerative performance of the implanted scaffolds was then analyzed at 4- and 8-weeks post-surgery, as illustrated in Figure 11A.

Micro-CT evaluation at 4- and 8-weeks post-implantation demonstrated notable differences in bone regeneration across the groups: Ctrl, DMPS, DMPS-PDA, and DMPS-PDA-EPO (Figure 11B). The control group showed minimal new bone formation, reflected by low BV/TV, Tb.N, and Tb.Th. In contrast, the DMPS-PDA-EPO group exhibited pronounced bone regeneration, especially at 8 weeks, with significantly increased BV/TV, Tb.N, and Tb.Th, along with decreased Tb.Sp and enhanced BMD. These results suggest that DMPS-PDA-EPO promotes the development of denser and higher-quality bone, demonstrating its strong osteoregenerative capability (Figure S19).

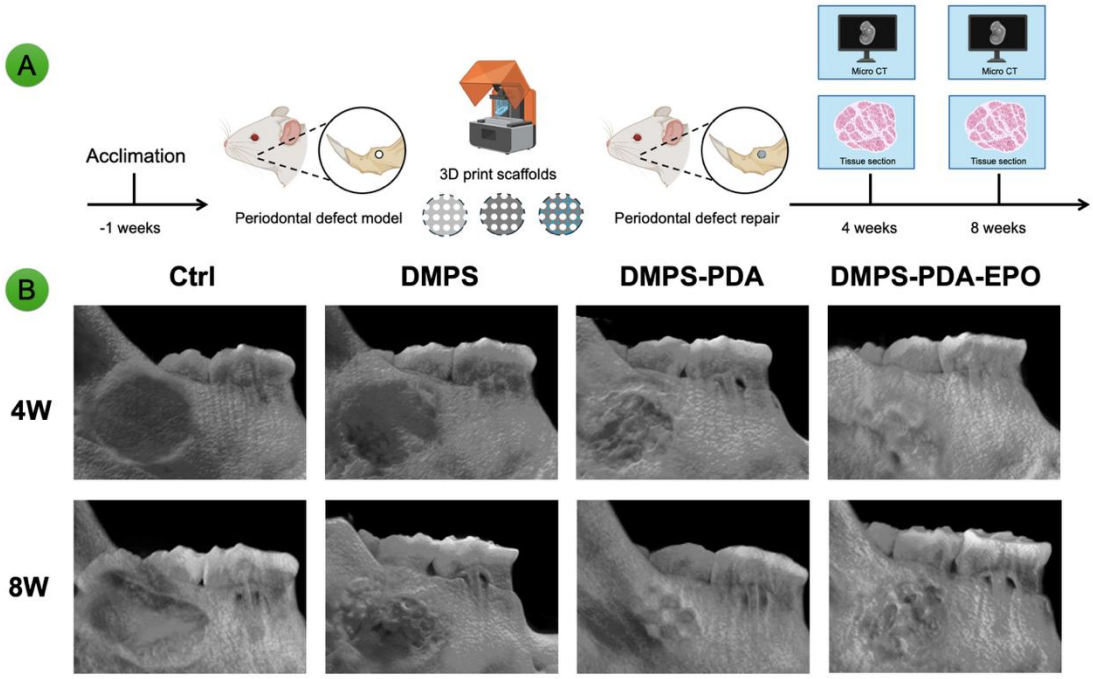

Figure 11. In vivo evaluation of DMPS-PDA-EPO–mediated bone regeneration in a rat periodontal fenestration defect model. (A) Schematic diagram illustrating the creation of the periodontal defect and implantation of DMPS, DMPS-PDA, and DMPS-PDA-EPO scaffolds. (B) Representative 3D Micro-CT reconstructions of rat jaws at 4- and 8-weeks post-surgery.

H&E and Masson's trichrome staining corroborated the micro-CT results (Figure 12). Histological examination showed that the control, DMPS, and DMPS-PDA groups exhibited limited bone regeneration, with incomplete defect closure and sparse new bone deposition. In contrast, the DMPS-PDA-EPO group demonstrated substantial new bone formation, particularly at 8 weeks, with a markedly higher amount of new alveolar bone effectively bridging the defect site.

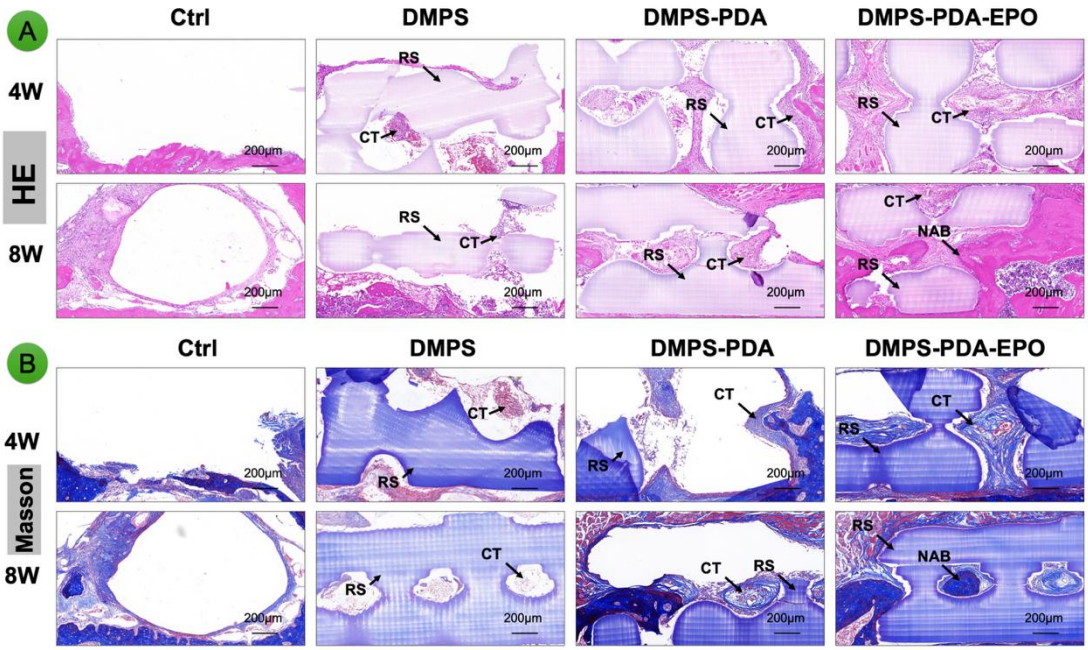

694

695 **Figure 12. Histology illustration images of the rat mandible.** (A) Histological
696 assessment of bone regeneration using H&E staining at 4 and 8 weeks. (B) Masson's
697 trichrome staining evaluation of bone formation at 4 and 8 weeks. NAB: denotes newly
698 formed alveolar bone; RS: residual scaffold; CT: connective tissue.

699 Immunohistochemical analysis of CD86 and CD206 revealed that CD206 expression
700 was markedly higher in the DMPS-PDA-EPO group compared to the control, DMPS,
701 and DMPS-PDA groups, whereas the number of CD86-positive cells was lower in the
702 DMPS-PDA-EPO group (Figure 13, S21A and S21B). These in vivo findings indicate
703 that DMPS-PDA-EPO suppresses M1 macrophage polarization while promoting M2
704 polarization. Given that excessive and prolonged M1 activation is a major contributor
705 to inflammation-induced alveolar bone resorption, this macrophage phenotype
706 transition suggests that the scaffold effectively mitigates the inflammatory
707 microenvironment at the early regenerative stage. Such immunomodulation is
708 consistent with the observed reduction of pro-inflammatory cytokines in vitro and is

closely associated with the subsequent enhancement of angiogenesis and osteogenesis in vivo, supporting a causal link between inflammation regulation and improved bone regeneration.

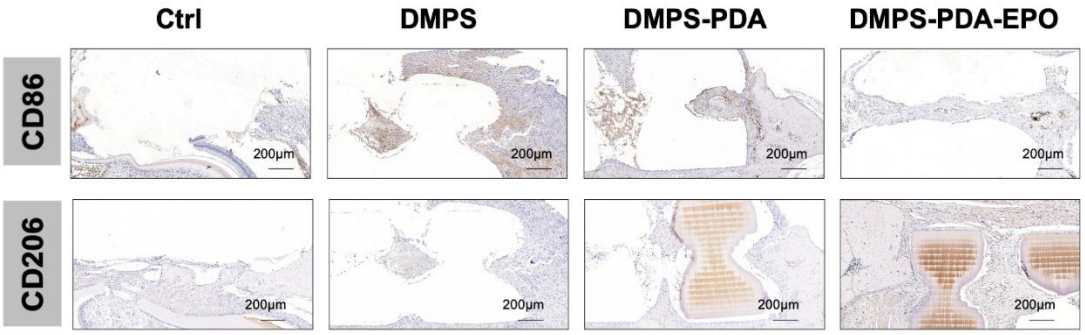

Figure 13. Immunohistochemistry images and statistical analysis of the rat mandibular sections for CD86 and CD206.

Immunohistochemical analysis of VEGF showed a significantly larger positive staining area in the DMPS-PDA-EPO group at 4 weeks, which gradually decreased by 8 weeks (Figure 14, S20 and S21C). Likewise, OCN staining demonstrated that DMPS-PDA-EPO exhibited the highest expression at 8 weeks, indicating its contribution to late-stage osteogenesis (Figure 14, S20 and S21D). These results suggest that DMPS-PDA-EPO promotes bone regeneration by enhancing early-phase vascularization and supporting subsequent bone mineralization. Overall, the DMPS-PDA-EPO group achieved superior regenerative outcomes compared to the other groups, correlating with

elevated VEGF-mediated angiogenesis and increased OCN-associated bone formation.

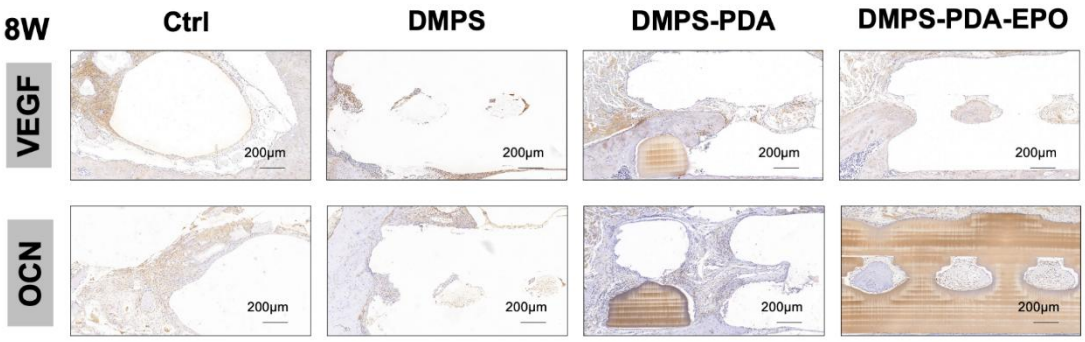

Figure 14. Immunohistochemistry images of the rat mandibular sections for VEGF and OCN at 8 weeks.

Systemic biosafety of DMPS-PDA-EPO was evaluated through H&E staining of major organs, including the heart, liver, spleen, lungs, and kidneys. No histological abnormalities or tissue damage were detected in any of the groups, indicating that the scaffold is biocompatible and safe for in vivo application (Figure S22).

A prominent feature of natural bone tissue is its highly interconnected porous architecture, which provides cells with a rich and diverse signaling environment that regulates their proliferation, differentiation, and fate determination. Current biomaterial scaffold designs for bone repair aim to replicate this microenvironment, thereby supporting cellular growth, osteogenic differentiation, and associated vascular formation. Consequently, three-dimensional hierarchical scaffolds with porous nanostructures are considered among the most promising candidates for bone substitutes. When constructing bone substitute scaffolds, a range of physical parameters must be taken into account, including porosity, pore size and architecture, surface roughness, compressive modulus, and the spatial arrangement of the ECM relative to

741 bone cells45. Various strategies have been developed for fabricating three-dimensional
742 porous scaffolds. Phase separation techniques offer a distinct advantage, as they allow
743 precise control over pore density, size, morphology, and interconnectivity by adjusting
744 multiple parameters such as polymer concentration, choice of solvent, and additives.
745 For example, Blaker et al. employed the thermally induced phase separation method
746 to fabricate highly porous PLGA microspheres with anisotropic channel structures and
747 hierarchical internal architecture, which enhance drug release and tissue
748 regeneration46. Similarly, Lei et al. used phase separation to produce nanofibrous
749 gelatin–silica composite scaffolds that closely mimic the physical structure, chemical
750 composition, and biological functions of the bone extracellular matrix47.

751 Pore architecture is a critical factor in the design of bone scaffolds. Numerous studies
752 have demonstrated that porosity not only provides space for osteogenic cell migration
753 and proliferation but also facilitates the transport of nutrients and metabolic waste,
754 while supporting angiogenesis48. Well-interconnected pores therefore promote cell
755 infiltration and efficient exchange of nutrients and waste products. Pore parameters—
756 such as pore size, porosity, and interconnectivity—have a significant impact on cellular
757 behavior49. In general, larger pores facilitate vascular ingrowth and the formation of a
758 well-oxygenated environment, promoting the generation of mineralized bone tissue,
759 whereas smaller pores offer more adsorption sites for bioactive molecules, enhancing
760 nutrient transport and waste removal. Optimal pore diameters are usually maintained
761 between 50–250 μm to maximize osteogenic effects. For instance, Petersen et al.
762 fabricated scaffolds with uniform pore sizes of 89 ± 15 μm, which significantly

improved cell migration depth50. Kim et al. produced hierarchical scaffolds with varying porosity and pore structures via self-curing combined with salt leaching, finding that micro-scale pores (approximately 3–25 μm) could induce new bone maturation and remodeling51. High-porosity scaffolds provide greater surface area, favoring the adsorption of bone-inductive proteins, ion exchange, and hydroxyapatite deposition, while the porous surface enhances cell proliferation and differentiation. Furthermore, interconnected pores serve as channels for cellular ingrowth. Viswanathan et al. synthesized scaffolds with both closed and open pore structures and found that pore interconnectivity regulated stem cell adhesion and differentiation52. Zhou et al. developed hierarchically interconnected scaffolds in which rational control of porosity and pore size enabled stem cells to proliferate and differentiate more actively, rapidly infiltrating the scaffold during osteogenesis53. In addition, pore structure and size influence cell morphology and macrophage migration, modulate autophagy activation, and thereby suppress inflammation while promoting osteogenesis54.

For maxillofacial and periodontal bone regeneration, effective scaffolds must exhibit sustained bioactivity and degradation kinetics compatible with the inflammatory and vascularized nature of the target tissue. The DMPS-PDA-EPO scaffold addresses these requirements by integrating hierarchical porosity with immuno-angiogenic biofunctionalization. The interconnected micro–macroporous architecture facilitates cell infiltration and mass transport, while PDA modification and sustained EPO release jointly regulate macrophage polarization, suppress oxidative stress, enhance endothelial

activity, and promote osteogenic differentiation, as consistently demonstrated in vitro and in vivo. Concurrently, the DEGDA-based scaffold shows slow and controlled degradation under physiological conditions, with stable pH during degradation, enabling the maintenance of mechanical support during early healing and gradual replacement by newly formed bone. Although direct quantitative assessment of in vivo scaffold degradation remains technically challenging for bulk three-dimensional implants, indirect evidence derived from micro-CT reconstruction and histological analyses provides insight into the degradation behavior of the DMPS-based scaffolds. In the rat periodontal defect model, progressive reduction in scaffold remnants was accompanied by increasing bone volume, trabecular thickness, and mineral density over time, suggesting gradual scaffold resorption concurrent with new bone formation. Histological staining further revealed intimate tissue–scaffold integration and progressive replacement of the implanted scaffold by newly formed alveolar bone, without signs of fibrous encapsulation or chronic inflammatory response. Importantly, H&E staining of major organs revealed no pathological abnormalities, suggesting that degradation products did not induce detectable systemic toxicity within the observation period. These results collectively support the biocompatible degradation behavior of the scaffold, while longer-term studies are warranted to fully elucidate its in vivo degradation kinetics and material fate.

Furthermore, a wide range of biomaterial systems have been developed for diabetic wound healing, a representative inflammation- and metabolism-impaired regenerative scenario, to address excessive inflammation, oxidative stress55, and insufficient

807 angiogenesis56. For instance, immunomodulatory biomaterials capable of reshaping
808 macrophage polarization and inflammatory signaling have been shown to significantly
809 enhance regenerative outcomes by restoring a pro-healing microenvironment5758.
810 Complementary strategies based on multifunctional surface chemistries and dynamic
811 cell–material interactions further demonstrate that precise regulation of inflammation
812 and oxidative stress is critical for coupling angiogenesis with tissue-specific
813 differentiation596061. Building upon these advances, the present DMPS-PDA-EPO
814 scaffold distinguishes itself by integrating hierarchical microporosity, intrinsic
815 antioxidant and immunoregulatory PDA chemistry, and sustained EPO delivery into a
816 unified hard-tissue–oriented platform. This multifunctional design enables
817 simultaneous modulation of inflammatory signaling, oxidative stress, angiogenesis, and
818 osteogenic differentiation under inflammatory conditions, thereby extending immune-
819 regenerative material concepts from predominantly soft tissue and wound healing
820 models toward inflammation-compromised bone regeneration scenarios. This high
821 level of functional integration and mechanistic synergy distinguishes the current system
822 from earlier platforms and underscores its broader applicability for inflammation-
823 compromised tissue regeneration beyond conventional wound healing models. From a
824 translational perspective, the DMPS-PDA-EPO scaffold shows strong potential for
825 clinical application in periodontal and alveolar bone defects, where persistent
826 inflammation, impaired angiogenesis, and insufficient osteogenesis coexist. The
827 modular macroporous design allows precise architectural control for defect adaptation,
828 while the DLP-based fabrication strategy ensures structural reproducibility, scalability,

and potential customization for patient-specific defects. Collectively, this work not only presents a promising therapeutic scaffold for complex inflammatory bone defects but also establishes a generalizable design paradigm that integrates immunomodulation, angiogenesis, and osteogenesis for advanced bone tissue engineering.

Conclusions

In this study, we developed a hierarchically interconnected porous scaffold via a dual-fabrication strategy, achieving architectural precision and mechanical robustness suitable for load-bearing periodontal applications. Polydopamine-mediated surface modification enabled efficient immobilization and sustained release of erythropoietin, endowing the scaffold with integrated immunomodulatory, angiogenic, and osteogenic functions. This multifunctional design promoted macrophage polarization toward a pro-healing M2 phenotype, enhanced neovascularization, and facilitated osteogenic differentiation, thereby establishing effective immune–vascular–bone coupling even under inflammatory conditions. In vivo results further confirmed significantly improved alveolar bone regeneration, characterized by increased bone volume, mineral density, and vascularized tissue ingrowth. From a translational perspective, the DMPS-PDA-EPO scaffold is well suited for clinically challenging periodontal and alveolar bone defects, where mechanical stability and immune-regenerative coordination are simultaneously required. The DLP-based fabrication strategy allows precise architectural control and scalable manufacturing, supporting defect-specific customization. Collectively, this work presents a mechanically stable and biologically

integrated scaffold platform with promising potential for clinical translation in inflammation-compromised bone regeneration.

Supporting Information:

Mechanical properties, diffusion properties, micro-CT, hydrophilicity, degradation experiment pH test, biocompatibility, wound healing assay and tube formation assay of HUVEC, Western blot semi-quantitative analysis, quantitative analysis of ALP activity, quantification of calcium deposition, quantitative analysis of bone parameters within the defect region, immunohistochemistry images and statistical analysis, assessment of scaffold toxicity in vivo and methods, including photographs of experimental setup.

AUTHOR INFORMATION

Corresponding Author

Weibin Sun, Department of Periodontics, Nanjing Stomatological Hospital, Affiliated Hospital of Medical School, Research Institute of Stomatology, Nanjing University, Nanjing, China.

Email: wbsun@nju.edu.cn

FuKe Wang, Institute of Materials Research and Engineering, A*STAR (Agency for Science, Technology and Research), Fusionopolis Way, Innovis, #08-03, Singapore 138634, Republic of Singapore.

Email: wangf@imre.a-star.edu.sg

Author Contributions

Xuan Zhang: Performed investigation, curated data, developed methodology, conducted formal analysis, and drafted the original manuscript. Jie Liu: Contributed to investigation and methodology. Yuyang Li: Assisted with methodology, investigation, and data curation. Wen Li: Provided software support, contributed to methodology, and assisted with data management. Deao Gu: Participated in investigation, data collection, and methodological development. Yi Ting Chong: Responsible for data acquisition related to compressive strength testing. Xuebin Yang: Contributed to manuscript revision and critical editing. FuKe Wang: Provided supervision, conceptual guidance, and manuscript review. Weibin Sun: Conceived the study, performed formal analysis, and contributed to manuscript reviewing and editing.

ACKNOWLEDGMENT

This work was supported by the National Natural Science Foundation of China (grant numbers. 51772144), the MTC Individual Research Grants (M23M6c0110) from A*STAR of Singapore, Medical Science and Technology Development Foundation, Nanjing Department of Health under (No. YKK24198, No. QNX25097), Nanjing University School of Medicine Graduate Practice Innovation Program (2025-7) and High-Level Hospital Construction Project of Nanjing Stomatological Hospital, Affiliated Hospital of Medical School, Institute of Stomatology, Nanjing University (No. 0224C020), Funded by Basic Research Program of Jiangsu Province (BK20250271).

Data availability

Data will be made available on request.

ABBREVIATIONS

EPO, Erythropoietin; PDA, polydopamine; DLP, digital light processing; BAPOs, Bisacylphosphine oxides; DEGDA, di(ethylene glycol) diacrylate; LPS, lipopolysaccharide; DA, Dopamine; DMEM, Dulbecco's modified Eagle medium; FBS, fetal bovine serum; PBS, phosphate-buffered saline; P/S, penicillin–streptomycin; STL, stereolithography; HUVECs, Human Umbilical Vein Endothelial Cells; hPDLSCs, human Periodontal Ligament Stem Cells; CCK-8, Cell Counting Kit-8; PI, propidium iodide; CLSM, confocal laser scanning microscope; ELISA, enzyme-linked immunosorbent assay; ROS, Reactive Oxygen Species; ALP, alkaline phosphatase; ARS, Alizarin Red S; GAPDH,Glyceraldehyde-3-phosphate dehydrogenase; BV/TV, bone volume fraction; Tb.N, trabecular number; Tb.Th, trabecular thickness; Tb.Sp, trabecular separation, BMD, bone mineral density; H&E, Hematoxylin & Eosin; OCN, osteocalcin; VEGF, vascular endothelial growth factor; TLC, thin-layer chromatography; IL-1,Interleukin-1 beta; COX-2, Cyclooxygenase-2; IL-6, Interleukin-6; IL-10, Interleukin-10; Arg-1, Arginase-1; TGF-β, Transforming Growth Factor-beta; TNF-α, Tumor Necrosis Factor-alpha; CCL, C-C motif chemokine ligand; VEGF, vascular endothelial growth factor; bFGF, basic fibroblast growth factor; EphB4, ephrin-B4 receptor; BMP2, bone morphogenetic protein 2; RunX2, runt-related transcription factor 2; GO, gene ontology; BP, biological processes; CC, cellular components; MF, molecular functions; ECM, extracellular matrix; KEGG, kyoto encyclopedia of genes and genomes; HIF-1, hypoxia-inducible factor 1; PI3K-Akt, phosphoinositide 3-kinase – protein kinase b; MAPK, mitogen-activated protein kinase; NAB, new alveolar bone. RS, residual scaffold; CT, connective tissue.

REFERENCES

(1) Daghrery, A.; Bottino, M. C. Advanced Biomaterials for Periodontal Tissue Regeneration. *genesis* **2022**, *60* (8–9), e23501. https://doi.org/10.1002/dvg.23501.

(2) Kanala, S.; Gudipalli, S.; Perumalla, P.; Jagalanki, K.; Polamarasetty, P.; Guntaka, S.; Gudala, A.; Boyapati, R. Aetiology, Prevalence, Fracture Site and Management of Maxillofacial Trauma. *Ann. R. Coll. Surg. Engl.* **2021**, *103* (1), 18–22. https://doi.org/10.1308/rcsann.2020.0171.

(3) Tan, B.; Tang, Q.; Zhong, Y.; Wei, Y.; He, L.; Wu, Y.; Wu, J.; Liao, J. Biomaterial-Based Strategies for Maxillofacial Tumour Therapy and Bone Defect Regeneration. *Int. J. Oral Sci.* **2021**, *13* (1), 9.

(4) Wu, H.; Li, Y.; Shi, L.; Liu, Y.; Shen, J. New Advances in Periodontal Functional Materials Based on Antibacterial, Anti-Inflammatory, and Tissue Regeneration Strategies. *Adv. Healthc. Mater.* **2025**, *14* (9), 2403206. https://doi.org/10.1002/adhm.202403206.

(5) Li, S.; Cai, X.; Guo, J.; Li, X.; Li, W.; Liu, Y.; Qi, M. Cell Communication and Relevant Signaling Pathways in Osteogenesis–Angiogenesis Coupling. *Bone Res.* **2025**, *13* (1), 45.

(6) Heimes, D.; Pabst, A.; Becker, P.; Hartmann, A.; Kloss, F.; Tunkel, J.; Smeets, R.; Kämmerer, P. W. Comparison of Morbidity-related Parameters between Autologous and Allogeneic Bone Grafts for Alveolar Ridge Augmentation from Patients' Perspective—A Questionnaire-based Cohort Study. *Clin. Implant Dent. Relat. Res.* **2024**, *26* (1), 170–182. https://doi.org/10.1111/cid.13242.

(7) Khademi, R.; Kharaziha, M. Recent Advances in Hydrogel-Based Platforms for Periodontal Tissue Regeneration. *Curr. Opin. Biomed. Eng.* **2025**, 100615.

(8) Ayala-Ham, A.; López-Gutierrez, J.; Bermúdez, M.; Aguilar-Medina, M.; Sarmiento-Sánchez, J. I.; López-Camarillo, C.; Sanchez-Schmitz, G.; Ramos-Payan, R. Hydrogel-Based Scaffolds in Oral Tissue Engineering. *Front. Mater.* **2021**, *8*, 708945.

(9) Chen, Y.; Dong, X.; Shafiq, M.; Myles, G.; Radacsi, N.; Mo, X. Recent Advancements on Three-Dimensional Electrospun Nanofiber Scaffolds for Tissue Engineering. *Adv. Fiber Mater.* **2022**, *4* (5), 959–986. https://doi.org/10.1007/s42765-022-00170-7.

(10) Du, X.; Dehghani, M.; Alsaadi, N.; Nejad, M. G.; Saber-Samandari, S.; Toghraie, D.; Su, C.-H.; Nguyen, H. C. A Femoral Shape Porous Scaffold Bio-Nanocomposite Fabricated Using 3D Printing and Freeze-Drying Technique for Orthopedic Application. *Mater. Chem. Phys.* **2022**, *275*, 125302.

(11) Dong, Z.; Cui, H.; Zhang, H.; Wang, F.; Zhan, X.; Mayer, F.; Nestler, B.; Wegener, M.; Levkin, P. A. 3D Printing of Inherently Nanoporous Polymers via Polymerization-Induced Phase Separation. *Nat. Commun.* **2021**, *12* (1), 247.

(12) Zhuang, Z.; Yoshizawa-Smith, S.; Glowacki, A.; Maltos, K.; Pacheco, C.; Shehabeldin, M.; Mulkeen, M.; Myers, N.; Chong, R.; Verdelis, K.; Garlet, G. P.; Little, S.; Sfeir, C. Induction of M2 Macrophages Prevents Bone Loss in Murine Periodontitis Models. *J. Dent. Res.* **2019**, *98* (2), 200–208. https://doi.org/10.1177/0022034518805984.

966 (13) Sun, X.; Gao, J.; Meng, X.; Lu, X.; Zhang, L.; Chen, R. Polarized
967 Macrophages in Periodontitis: Characteristics, Function, and Molecular Signaling.
968 *Front. Immunol.* **2021**, *12*, 763334.

969 (14) Yu, Y.; Ma, L.; Zhang, H.; Sun, W.; Zheng, L.; Liu, C.; Miao, L. EPO Could
970 Be Regulated by HIF-1 and Promote Osteogenesis and Accelerate Bone Repair. *Artif.*
971 *Cells Nanomedicine Biotechnol.* **2020**, *48* (1), 206–217.
972 https://doi.org/10.1080/21691401.2019.1699827.

973 (15) Gu, D.; Liu, H.; Qiu, X.; Yu, Y.; Tang, X.; Liu, C.; Miao, L. Erythropoietin
974 Induces Odontoblastic Differentiation of Human-derived Pulp Stem Cells via EphB4-
975 Mediated MAPK Signaling Pathway. *Oral Dis.* **2023**, *29* (7), 2816–2826.
976 https://doi.org/10.1111/odi.14486.

977 (16) Li, Y.; Peng, H.; Tang, W.; Gu, D.; Ren, S.; Yu, Y.; Yang, J.; Miao, L.
978 Accelerating Periodontal Regeneration through Injectable Hydrogel-Enabled
979 Sequential Delivery of Nanoceria and Erythropoietin. *Mater. Des.* **2023**, *225*, 111540.
980 https://doi.org/10.1016/j.matdes.2022.111540.

981 (17) Koushik, T. M.; Miller, C. M.; Antunes, E. Bone Tissue Engineering
982 Scaffolds: Function of Multi-Material Hierarchically Structured Scaffolds. *Adv.*
983 *Healthc. Mater.* **2023**, *12* (9), 2202766. https://doi.org/10.1002/adhm.202202766.

984 (18) Mapossa, A. B.; Tewo, R. K.; Ray, S. S.; Mhike, W.; Sundararaj, U. A Review
985 on Thermally Induced Phase Separation Technology in the Fabrication of Microporous
986 Polymer Membrane Devices for Sustained-repellent Delivery: Crystallization and

Morphological Studies. *J. Polym. Sci.* **2024**, *62* (23), 5205–5231. https://doi.org/10.1002/pol.20240232.

(19) Kang, J.; Hwang, J.-Y.; Huh, M.; Yun, S. I. Porous Poly(3-Hydroxybutyrate) Scaffolds Prepared by Non-Solvent-Induced Phase Separation for Tissue Engineering. *Macromol. Res.* **2020**, *28* (9), 835–843. https://doi.org/10.1007/s13233-020-8109-x.

(20) Xu, Y.; Tang, L.; Nok-iangthong, C.; Wagner, M.; Baumann, G.; Feist, F.; Bismarck, A.; Jiang, Q. Functionally Gradient Macroporous Polymers: Emulsion Templating Offers Control over Density, Pore Morphology, and Composition. *ACS Appl. Polym. Mater.* **2024**, *6* (9), 5150–5162. https://doi.org/10.1021/acsapm.4c00261.

(21) Sharma, A.; Ravindran, S.; Gupta, A. K. Fabrication and Mechanical Properties of Tri-Layer B_4 C-Reinforced Al–Zn Functionally Graded Foam Having Higher Energy Absorption Efficiency. *Adv. Eng. Mater.* **2023**, *25* (11), 2201734. https://doi.org/10.1002/adem.202201734.

(22) Wu, B.; Yuan, L.; Liu, M.; Tang, M.; Jiang, D.; Yi, Y.; Ma, S.; Yan, B.; Lu, Y. Construction of a Viscoelastic Model of Human Cancellous Bone in Alveolar Bone Based on Bone Mineral Density Distribution. *Materials* **2023**, *16* (23), 7427.

(23) Liu, L.; Kai, H.; Nagamine, K.; Ogawa, Y.; Nishizawa, M. Porous Polymer Microneedles with Interconnecting Microchannels for Rapid Fluid Transport. *RSC Adv.* **2016**, *6* (54), 48630–48635.

(24) Ma, T.; Wang, C.; Ge, X.; Zhang, Y. Applications of Polydopamine in Implant Surface Modification. *Macromol. Biosci.* **2023**, *23* (10), 2300067. https://doi.org/10.1002/mabi.202300067.

(25) Li, L.; Wu, R.; Hong, R.; Chen, X.; Huang, T.; Huang, S.; Mo, X.; Wang, Z.; Liu, W.; Lu, Y. Mussel-Inspired Integrated Functional 3D Printed Scaffolds with Molybdenum Disulfide Nanoflowers for Tumor Therapy and Bone Reconstruction. *Chem. Eng. J.* **2025**, *509*, 161399.

(26) Liu, W.; Wei, Y.; Zhang, X.; Xu, M.; Yang, X.; Deng, X. Lower Extent but Similar Rhythm of Osteogenic Behavior in hBMSCs Cultured on Nanofibrous Scaffolds *versus* Induced with Osteogenic Supplement. *ACS Nano* **2013**, *7* (8), 6928–6938. https://doi.org/10.1021/nn402118s.

(27) Feng, J.; Liu, J.; Wang, Y.; Diao, J.; Kuang, Y.; Zhao, N. Beta-TCP Scaffolds with Rationally Designed Macro-Micro Hierarchical Structure Improved Angio/Osteo-Genesis Capability for Bone Regeneration. *J. Mater. Sci. Mater. Med.* **2023**, *34* (7), 36. https://doi.org/10.1007/s10856-023-06733-3.

(28) Ghorai, S. K.; Dutta, A.; Roy, T.; Guha Ray, P.; Ganguly, D.; Ashokkumar, M.; Dhara, S.; Chattopadhyay, S. Metal Ion Augmented Mussel Inspired Polydopamine Immobilized 3D Printed Osteoconductive Scaffolds for Accelerated Bone Tissue Regeneration. *ACS Appl. Mater. Interfaces* **2022**, *14* (25), 28455–28475. https://doi.org/10.1021/acsami.2c01657.

(29) Liu, H.; Wang, C.; Sun, X.; Zhan, C.; Li, Z.; Qiu, L.; Luo, R.; Liu, H.; Sun, X.; Li, R.; Zhang, J. Silk Fibroin/Collagen/Hydroxyapatite Scaffolds Obtained by 3D Printing Technology and Loaded with Recombinant Human Erythropoietin in the Reconstruction of Alveolar Bone Defects. *ACS Biomater. Sci. Eng.* **2022**, *8* (12), 5245–5256. https://doi.org/10.1021/acsbiomaterials.2c00690.

(30) Du, Y.; Guo, J. L.; Wang, J.; Mikos, A. G.; Zhang, S. Hierarchically Designed Bone Scaffolds: From Internal Cues to External Stimuli. *Biomaterials* **2019**, *218*, 119334.

(31) Li, T.; Ma, H.; Ma, H.; Ma, Z.; Qiang, L.; Yang, Z.; Yang, X.; Zhou, X.; Dai, K.; Wang, J. Mussel-Inspired Nanostructures Potentiate the Immunomodulatory Properties and Angiogenesis of Mesenchymal Stem Cells. *ACS Appl. Mater. Interfaces* **2019**, *11* (19), 17134–17146. https://doi.org/10.1021/acsami.8b22017.

(32) Sloniak, M. C.; Lepique, A. P.; Nakao, L. Y. S.; Villar, C. C. Alterations in Macrophage Polarization Play a Key Role in Control and Development of Periodontal Diseases. *J. Indian Soc. Periodontol.* **2023**, *27* (6), 578–582.

(33) Peng, S.; Fu, H.; Li, R.; Li, H.; Wang, S.; Li, B.; Sun, J. A New Direction in Periodontitis Treatment: Biomaterial-Mediated Macrophage Immunotherapy. *J. Nanobiotechnology* **2024**, *22* (1), 359. https://doi.org/10.1186/s12951-024-02592-4.

(34) Zou, Y.; Xie, Q.; Lin, J.; Dong, H.; Zhuang, X.; Xian, R.; Liang, Y.; Li, S. Immunomodulatory Effects and Mechanisms of Two-Dimensional Black Phosphorus

on Macrophage Polarization and Bone Regeneration. *Int. J. Nanomedicine* **2025**, *Volume 20*, 4337–4355. https://doi.org/10.2147/IJN.S508309.

(35) Abedi, N.; Sadeghian, A.; Kouhi, M.; Haugen, H. J.; Savabi, O.; Nejatidanesh, F. Immunomodulation in Bone Tissue Engineering: Recent Advancements in Scaffold Design and Biological Modifications for Enhanced Regeneration. *ACS Biomater. Sci. Eng.* **2025**, *11* (3), 1269–1290. https://doi.org/10.1021/acsbiomaterials.4c01613.

(36) He, Z.; Sun, C.; Ma, Y.; Chen, X.; Wang, Y.; Chen, K.; Xie, F.; Zhang, Y.; Yuan, Y.; Liu, C. Rejuvenating Aged Bone Repair through Multihierarchy Reactive Oxygen Species-Regulated Hydrogel. *Adv. Mater.* **2024**, *36* (9), 2306552. https://doi.org/10.1002/adma.202306552.

(37) Yuan, X.; Zhu, W.; Yang, Z.; He, N.; Chen, F.; Han, X.; Zhou, K. Recent Advances in 3D Printing of Smart Scaffolds for Bone Tissue Engineering and Regeneration. *Adv. Mater.* **2024**, *36* (34), 2403641. https://doi.org/10.1002/adma.202403641.

(38) Xu, Z.; Wang, B.; Huang, R.; Guo, M.; Han, D.; Yin, L.; Zhang, X.; Huang, Y.; Li, X. Efforts to Promote Osteogenesis–Angiogenesis Coupling for Bone Tissue Engineering. *Biomater. Sci.* **2024**, *12* (11), 2801–2830.

(39) Hao, S.; Zhou, D.; Wang, F.; Li, G.; Deng, A.; Ren, X.; Wang, X.; Jing, Y.; Shi, Z.; Bai, L. Hamburger-like Biomimetic Nutrient Periosteum with Osteoimmunomodulation, Angio-/Osteo-Genesis Capacity Promoted Critical-Size Bone Defect Repair. *Chem. Eng. J.* **2024**, *489*, 150990.

(40) Peng, B.; Kong, G.; Yang, C.; Ming, Y. Erythropoietin and Its Derivatives: From Tissue Protection to Immune Regulation. *Cell Death Dis.* **2020**, *11* (2), 79.

(41) Sun, Z.; Zhao, H. Mechanism of Erythropoietin/Erythropoietin Receptor Signaling Pathway in Regulating Osteogenic Differentiation of Periodontal Ligament Stem Cells. *Chin. J. Tissue Eng. Res.* **2025**, *29* (36), 7762.

(42) de Sá Pereira, I. O. N. The Effect of Erythropoietin in the Nonsurgical Treatment of Periodontitis-A Systematic Review. *PQDT-Glob.* **2023**.

(43) Wu, Y.; Wang, X.; Zhang, Y.; Wen, Z.; Li, Y.; Zhang, K.; Gosar, N.; Li, Q.; Mao, J.; Gong, S. Proanthocyanidins Ameliorate LPS-Inhibited Osteogenesis of PDLSCs by Restoring Lysine Lactylation. *Int. J. Mol. Sci.* **2024**, *25* (5), 2947.

(44) Golafshan, N.; Castilho, M.; Daghrery, A.; Alehosseini, M.; Van De Kemp, T.; Krikonis, K.; De Ruijter, M.; Dal-Fabbro, R.; Dolatshahi-Pirouz, A.; Bhaduri, S. B.; Bottino, M. C.; Malda, J. Composite Graded Melt Electrowritten Scaffolds for Regeneration of the Periodontal Ligament-to-Bone Interface. *ACS Appl. Mater. Interfaces* **2023**, *15* (10), 12735–12749. https://doi.org/10.1021/acsami.2c21256.

(45) Reznikov, N.; Boughton, O. R.; Ghouse, S.; Weston, A. E.; Collinson, L.; Blunn, G. W.; Jeffers, J. R.; Cobb, J. P.; Stevens, M. M. Individual Response Variations in Scaffold-Guided Bone Regeneration Are Determined by Independent Strain-and Injury-Induced Mechanisms. *Biomaterials* **2019**, *194*, 183–194.

(46) Blaker, J. J.; Knowles, J. C.; Day, R. M. Novel Fabrication Techniques to Produce Microspheres by Thermally Induced Phase Separation for Tissue Engineering and Drug Delivery. *Acta Biomater.* **2008**, *4* (2), 264–272.

(47) Lei, B.; Shin, K.-H.; Noh, D.-Y.; Jo, I.-H.; Koh, Y.-H.; Choi, W.-Y.; Kim, H.-E. Nanofibrous Gelatin–Silica Hybrid Scaffolds Mimicking the Native Extracellular Matrix (ECM) Using Thermally Induced Phase Separation. *J. Mater. Chem.* **2012**, *22* (28), 14133–14140.

(48) Mohammadi, H.; Sepantafar, M.; Muhamad, N.; Bakar Sulong, A. How Does Scaffold Porosity Conduct Bone Tissue Regeneration? *Adv. Eng. Mater.* **2021**, *23* (10), 2100463. https://doi.org/10.1002/adem.202100463.

(49) Hernandez, J. L.; Woodrow, K. A. Medical Applications of Porous Biomaterials: Features of Porosity and Tissue-Specific Implications for Biocompatibility. *Adv. Healthc. Mater.* **2022**, *11* (9), 2102087. https://doi.org/10.1002/adhm.202102087.

(50) Petersen, A.; Princ, A.; Korus, G.; Ellinghaus, A.; Leemhuis, H.; Herrera, A.; Klaumünzer, A.; Schreivogel, S.; Woloszyk, A.; Schmidt-Bleek, K. A Biomaterial with a Channel-like Pore Architecture Induces Endochondral Healing of Bone Defects. *Nat. Commun.* **2018**, *9* (1), 4430.

(51) Kim, J.-A.; Lim, J.; Naren, R.; Yun, H.; Park, E. K. Effect of the Biodegradation Rate Controlled by Pore Structures in Magnesium Phosphate Ceramic Scaffolds on Bone Tissue Regeneration in Vivo. *Acta Biomater.* **2016**, *44*, 155–167.

(52) Viswanathan, P.; Ondeck, M. G.; Chirasatitsin, S.; Ngamkham, K.; Reilly, G. C.; Engler, A. J.; Battaglia, G. 3D Surface Topology Guides Stem Cell Adhesion and Differentiation. *Biomaterials* **2015**, *52*, 140–147.

(53) Zhu, L.; Luo, D.; Liu, Y. Effect of the Nano/Microscale Structure of Biomaterial Scaffolds on Bone Regeneration. *Int. J. Oral Sci.* **2020**, *12* (1), 6. https://doi.org/10.1038/s41368-020-0073-y.

(54) Chen, Z.; Ni, S.; Han, S.; Crawford, R.; Lu, S.; Wei, F.; Chang, J.; Wu, C.; Xiao, Y. Nanoporous Microstructures Mediate Osteogenesis by Modulating the Osteo-Immune Response of Macrophages. *Nanoscale* **2017**, *9* (2), 706–718.

(55) Yan, Z.; Zhang, Y.; Chen, Q.; Li, J.; Ning, X.; Bai, F.; Wang, Y.; Liu, X.; Liu, Y.; Zhang, M. Carbon Dot Superoxide Dismutase Nanozyme Enhances Reactive Oxygen Species Scavenging in Diabetic Skin Wound Repair. *J. Adv. Res.* **2025**.

(56) Deng, Q.; Du, F.; Pan, S.; Xia, Y.; Zhu, Y.; Zhang, J.; Li, C.; Yu, S. Activation of Angiopoietin-1 Signaling with Engineering Mesenchymal Stem Cells Promoted Efficient Angiogenesis in Diabetic Wound Healing. *Stem Cell Res. Ther.* **2025**, *16* (1), 75. https://doi.org/10.1186/s13287-025-04207-7.

(57) Wu, M.; Liu, H.; Zhu, Y.; Chen, F.; Chen, Z.; Guo, L.; Wu, P.; Li, G.; Zhang, C.; Wei, R.; Cai, L. Mild Photothermal-Stimulation Based on Injectable and Photocurable Hydrogels Orchestrates Immunomodulation and Osteogenesis for High-Performance Bone Regeneration. *Small* **2023**, *19* (28), 2300111. https://doi.org/10.1002/smll.202300111.

(58) Wu, M.; Liu, H.; Li, D.; Zhu, Y.; Wu, P.; Chen, Z.; Chen, F.; Chen, Y.; Deng, Z.; Cai, L. Smart-Responsive Multifunctional Therapeutic System for Improved Regenerative Microenvironment and Accelerated Bone Regeneration via Mild Photothermal Therapy. *Adv. Sci.* **2024**, *11* (2), 2304641. https://doi.org/10.1002/advs.202304641.

(59) Zhu, Y.; Liu, H.; Wu, P.; Chen, Y.; Deng, Z.; Cai, L.; Wu, M. Multifunctional Injectable Hydrogel System as a Mild Photothermal-Assisted Therapeutic Platform for Programmed Regulation of Inflammation and Osteo-Microenvironment for Enhanced Healing of Diabetic Bone Defects *in Situ*. *Theranostics* **2024**, *14* (18), 7140–7198. https://doi.org/10.7150/thno.102779.

(60) Yang, Z.; Zhu, Y.; Cheng, J.; Chen, Y.; Wu, P.; Liu, X.; Cai, L.; Du, L.; Wu, M. Polyphenol-Derived Nanoarmor-Functionalized Photothermal Hydrogel Platform for Programmed Modulation of the Regenerative Microenvironment and Bone Defect Healing. *Small* **2025**, e10733. https://doi.org/10.1002/smll.202510733.

(61) Wu, M.; Liu, H.; Zhu, Y.; Wu, P.; Chen, Y.; Deng, Z.; Zhu, X.; Cai, L. Bioinspired Soft-Hard Combined System with Mild Photothermal Therapeutic Activity Promotes Diabetic Bone Defect Healing via Synergetic Effects of Immune Activation and Angiogenesis. *Theranostics* **2024**, *14* (10), 4014–4057. https://doi.org/10.7150/thno.97335.